

Chapter 5

AHTR Modeling and Optimization Methodology

In this chapter, I describe the modeling and optimization methodology of the Advanced High-Temperature Reactor (AHTR) optimization for non-conventional geometries and parameters conducted using Reactor evOLutionary aLgorithm Optimizer (ROLLO). The optimization tool should enable the placement of fuel, moderation, and coolant material in any possible location, within physical limits, to wholly explore the design space enabled by additive manufacturing. Since exploring non-conventional geometries and parameters has barely been attempted (previous attempts described in Section 2.3.2), this dissertation does one of the first goes at beginning to explore the large design space. The work done for this dissertation is only an intermediate step towards developing a truly arbitrary geometry expression.

The subsequent sections define the optimization problem definitions, describe the AHTR geometries, outline the AHTR modeling workflow, verify the AHTR models, and describe the process of tuning ROLLO’s hyperparameters for the optimization problems.

5.1 ROLLO Optimization Problem Definitions

In an effort toward optimizing the AHTR design for non-conventional geometries and parameters. I chose to vary the following AHTR parameters:

- Tristructural Isotropic (TRISO) packing fraction distribution ($\rho_{TRISO}(\vec{r})$)
- Total fuel packing fraction
- Fluoride-Lithium-Beryllium (FLiBe) coolant channel shape

The TRISO packing fraction distribution variation enables exploration of how heterogeneous fuel distributions impact reactor performance. In Section 3.3.1, the Fluoride-Salt-Cooled High-Temperature Reactor (FHR) benchmark results demonstrated that increased fuel packing does not always correspond with increased k_{eff} due to self-shielding effects. Varying total fuel packing fraction and TRISO distribution synergistically enable exploration of how heterogenous TRISO distribution could minimize self-shielding and thus, reduce the fuel required for a reactor design. The FLiBe coolant channel shape variation enables exploration of how non-uniform channel shapes impact reactor performance.

I selected three key AHTR optimization objectives that address contrasting reactor core qualities. Table 5.1 describes each objective, how I quantified them, and the motivation.

Table 5.1: Reactor evOLutionary aLgorithm Optimizer (ROLLO) Advanced High-Temperature Reactor (AHTR) optimization problem objectives with their quantification descriptions and motivation.

Objective	Quantification	Motivation
Minimize fuel amount	Minimize total fuel packing fraction	Cost savings, Non-proliferation
Maximize heat transfer	Minimize maximum temperature	Enable the system to perform at a higher power with minimized thermal stress
Minimize power peaking	Minimize power peaking factor normalized by fuel distribution	Efficient fuel utilization, longer core life, safety

To optimize the described objectives, I will vary the described parameters in the AHTR plank and one-third assembly models. The optimization results for the AHTR plank and one-third assembly models are reported in Chapters 6 and 7, respectively. The plank optimization is a preliminary study to inform the more complex AHTR one-third assembly optimization setup. In the next section, I will describe both geometries.

5.2 AHTR Geometry for Optimization Problem

I apply the optimization process to the AHTR plank and AHTR one-third assembly geometries. The geometries are adapted from the FHR benchmark's AHTR design, outlined in Chapter 3 (see Figure 3.2). The main differences occur in the fuel plank region. In the FHR benchmark, the TRISO particles are arranged in rectangular lattices within two fuel stripes in the fuel plank region. For the optimization problems, I discretized each plank into ten cells with random TRISO packing and an individually controlled packing fraction. Thus, the AHTR plank has ten fuel cells, and the AHTR one-third assembly has 60 fuel cells. The subsequent subsections describe each geometry in further detail. I also omit the graphite spacers.

5.2.1 AHTR Plank Geometry

The AHTR plank is a single graphite fuel plank model from the AHTR design (Figure 3.2). I modified the fuel plank to be straightened with perpendicular sides instead of slanted as in Figure 3.4 for ease of modeling. The one-third assembly optimization uses the original slanted AHTR planks. Figure 5.1 illustrates the straightened fuel plank with ten fuel cells with random TRISO packing. The plank has $27.1 \times 3.25 \times 1.85 \text{ cm}^3$ dimensions with reflective

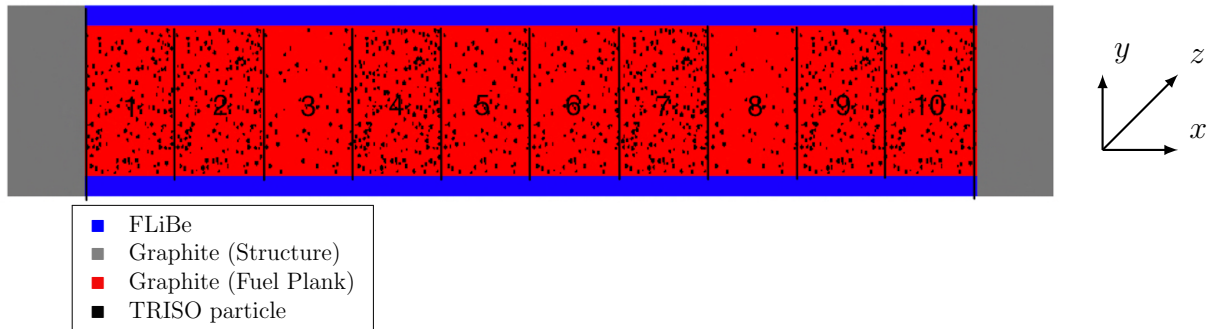


Figure 5.1: Straightened Advanced High-Temperature Reactor (AHTR) fuel plank with 10 fuel cells with random TRISO packing, graphite buffers, and FLiBe coolant channels. This geometry is used for AHTR plank optimization. Original slanted fuel planks can be seen in Figures 3.2 and 3.4.

boundary conditions.

I used the same materials as in the FHR benchmark (Chapter 3), except that I homogenized each TRISO particle's four outer layers: porous carbon buffer, inner pyrolytic carbon, silicon carbide layer, and the outer pyrolytic carbon. The TRISO particle dimensions remain the same. Table 5.2 reports OpenMC's k_{eff} for the straightened AHTR configuration with and without the outer layer TRISO homogenization.

Table 5.2: Straightened Advanced High-Temperature Reactor (AHTR) fuel plank k_{eff} for the case with no TRISO homogenization and case with homogenization of the four outer layers. Both simulations were run on one BlueWaters XE Node.

TRISO Homogenization	k_{eff}	Simulation time [s]
None	1.38548 ± 0.00124	233
Four outer layers	1.38625 ± 0.00109	168

The TRISO particle outer four-layer homogenization resulted in a 30% speed-up without compromising accuracy with k_{eff} values within each other's uncertainty.

5.2.2 AHTR One-Third Assembly Geometry

The AHTR one-third assembly is one-diamond shape sector of the AHTR assembly. The one-third assembly contains six graphite fuel planks. Each graphite fuel plank has graphite buffers and ten rectangular prism fuel cells with random TRISO packing and individually controlled packing fractions. Figure 5.2 shows the one-third AHTR assembly with 10 x 6 fuel cells with random TRISO packing. The one-third assembly model has reflective boundary conditions and uses the TRISO particle outer four-layer homogenization described in Section 5.2.1.

5.3 AHTR Model Workflow

The ROLLO software drives the evolutionary algorithm optimization process, depicted in Figure 4.1. In a ROLLO input file, I define control variables for the genetic algorithm to vary.

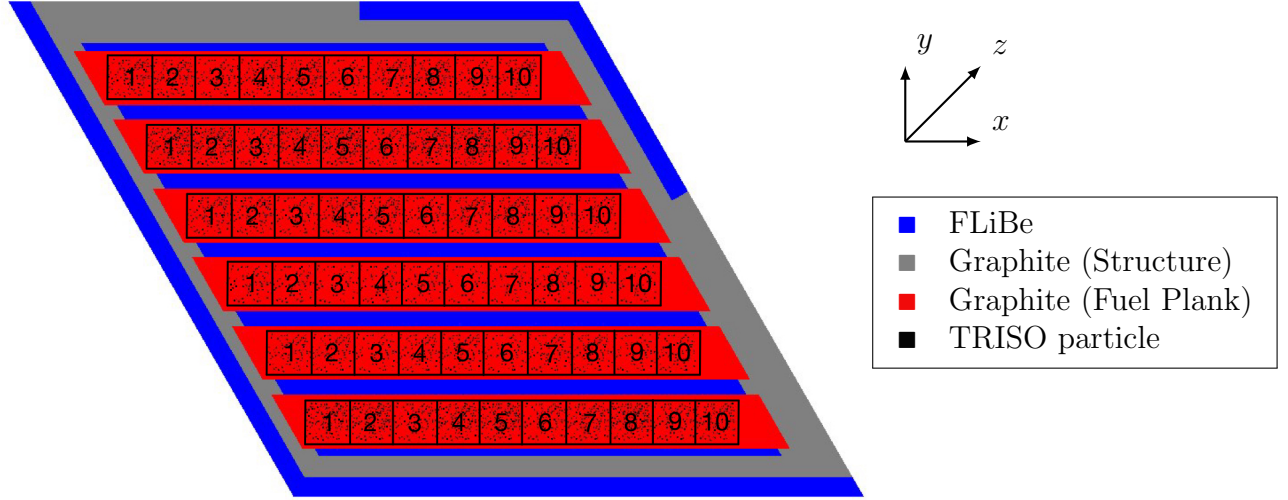


Figure 5.2: Advanced High-Temperature Reactor (AHTR) one-third assembly with ten fuel cells in each graphite plank with random TRISO packing, graphite structure, and FLiBe coolant. Original FHR benchmark fuel assembly with fuel stripes can be seen in Figure 3.2.

These control variables control the AHTR parameters described in Section 5.1. The control variables are input into the nuclear software templates to model different AHTR geometries. The nuclear software will then run the AHTR models and calculate the optimization objective and constraint values. In this work, I use OpenMC [74] to model AHTR’s neutronics and Moltres [55] to model the AHTR’s multi-physics. Descriptions of each software can be found in Section 2.1.4.

In the following subsections, I describe the AHTR modeling workflow: the AHTR input parameter variations, the OpenMC and Moltres models, and the output and constraint values calculations. The AHTR modeling workflow described in this section falls within the *evaluate population* orange blocks in Figure 4.1’s genetic algorithm flow chart. Figure 5.3 illustrates the AHTR modeling workflow.

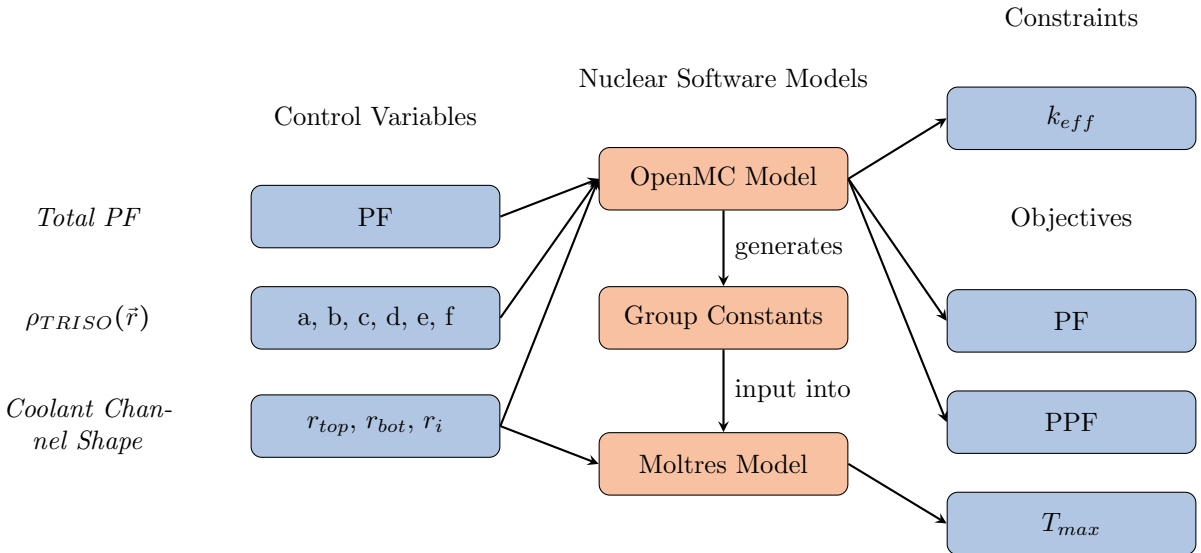


Figure 5.3: Advanced High-Temperature Reactor (AHTR) modeling workflow in Reactor evOLutionary aLgorithm Optimizer (ROLLO) optimization. The entire workflow falls within the 'evaluate population' orange blocks in ROLLO's evolutionary algorithm optimization process depicted in Figure 4.1. For each reactor model in the optimization process, the modeling workflow begins with ROLLO selecting the control variables. ROLLO inserts control parameters into templated OpenMC and Moltres input files. The OpenMC and Moltres models are run. ROLLO analyzes the OpenMC and Moltres output files to determine constraint and objective values. PF: Total packing fraction, $\rho_{TRISO}(\vec{r})$: TRISO packing fraction distribution, PPF: normalized power peaking factor, T_{max} : model's maximum temperature.

5.3.1 Input Parameter Modeling

This section describes how I model the AHTR input parameter variations: total fuel packing fraction, TRISO packing fraction distribution, and FLiBe coolant channel shape. For both the AHTR plank and one-third assembly models, the total fuel packing fraction parameter is a single numerical input. In the subsequent subsections, I describe how I modeled the other two parameters for the AHTR plank and one-third assembly models.

Input Parameter Modeling: TRISO packing fraction distribution

I utilize sine distributions for both the AHTR plank and one-third assembly models to govern the TRISO packing fraction distribution. Based on the sine distributions, the model calculates each fuel cell's packing fraction, then uses OpenMC's `pack_spheres` function to randomly disperse the packing fraction in each fuel cell. For the AHTR plank, one sine distribution governs the TRISO packing fraction distribution across the AHTR plank's x-direction. For the AHTR one-third assembly, two sine distributions govern the TRISO packing fraction distribution across each fuel plank's x-direction and the assembly's y-direction, respectively.

For the AHTR plank, Equation 5.1's sine distribution governs the TRISO packing fraction distribution across the ten fuel cells in the x-direction:

$$PF(x) = (a \cdot \sin(b \cdot x + c) + 2) \cdot NF \quad (5.1)$$

where

$PF(x)$ = packing fraction distribution across ten cells [-]

a = amplitude, peak deviation of the function from zero [-]

b = angular frequency, rate of change of the function argument [$\frac{\text{radians}}{\text{cm}}$]

c = phase, the position in its cycle the oscillation is at $t = 0$ [radians]

x = midpoint value for each cell [cm]

NF = normalization factor [-]

Figure 5.1 depicts the ten fuel cells. The sine distribution's coefficients, $a b c$, are the control variables ROLLO utilizes to control the plank's TRISO packing fraction distribution. Thus, ROLLO will vary a, b, c variables to find an optimal TRISO particle sine distribution. The normalization factor normalizes the TRISO distribution based on the defined total packing fraction.

An AHTR plank with a 0.0979 total packing fraction, and packing fraction distribution of $PF(x) = (0.5 \cdot \sin(\frac{\pi}{3} \cdot x + \pi) + 2) \cdot NF$, results in the following packing fractions for the ten cells: 0.103, 0.120, 0.049, 0.138, 0.076, 0.081, 0.136, 0.048, 0.125, and 0.098. Figure 5.4 shows this sine distribution, highlights the packing fraction at the respective midpoints, and displays the plank's x-y axis view with the packing fraction varying based on this sine distribution.

For the AHTR one-third assembly, Equation 5.2's two sine distributions govern TRISO packing fraction distributions in the x and y direction for the 10 x 6 fuel cells:

$$PF(x, y) = (a \cdot \sin(b \cdot x + c) + 2) \cdot (d \cdot \sin(e \cdot y + f) + 2) \cdot NF \quad (5.2)$$

where

$PF(x, y)$ = packing fraction distribution across 60 cells [-]

a, d = amplitude, peak deviation of the function from zero [-]

b, e = angular frequency, rate of change of the function argument [$\frac{\text{radians}}{\text{cm}}$]

c, f = phase, the position in its cycle the oscillation is at $t = 0$ [radians]

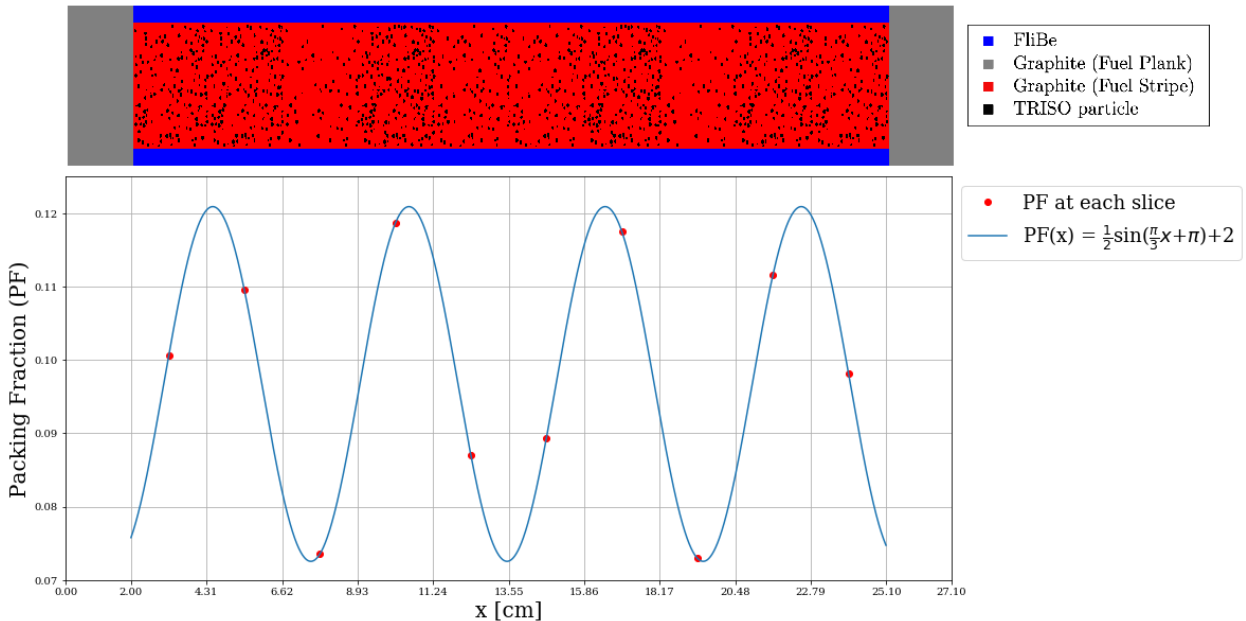


Figure 5.4: Above: Straightened Advanced High-Temperature Reactor (AHTR) fuel plank with varying TRISO particle distribution across ten cells based on the sine distribution. Below: $PF(x) = (0.5 \sin(\frac{\pi}{3}x + \pi) + 2) \times NF$ sine distribution with red points indicating the packing fraction at each cell.

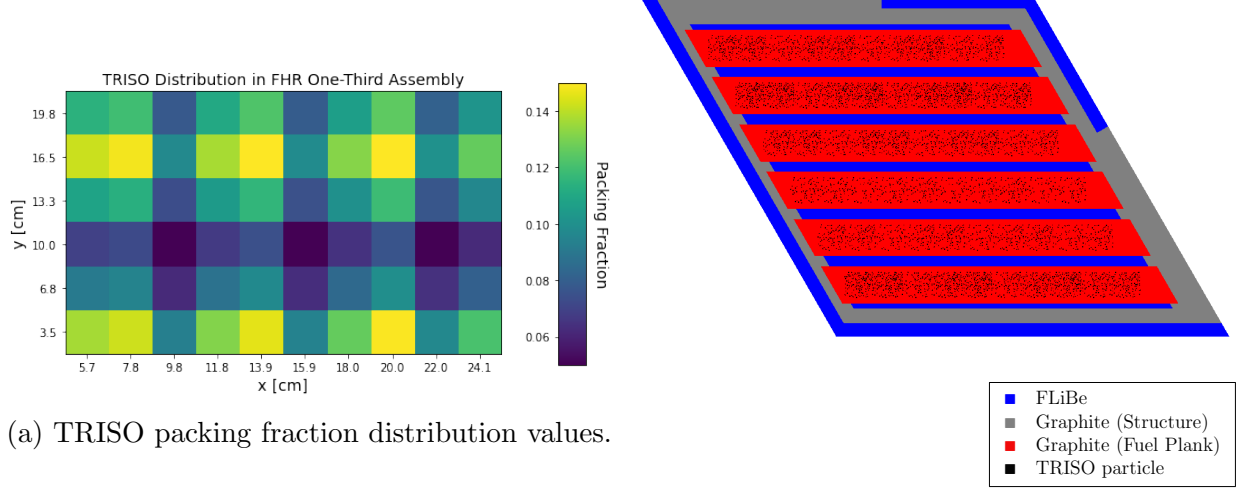
x = midpoint value for each x-direction fuel cell [cm]

y = midpoint value for each fuel plank [cm]

NF = normalization factor [-]

Figure 5.2 depicts the 10 x 6 fuel cells. The sine distribution's coefficients, $a b c d e f$, are the control variables ROLLO utilizes to control the TRISO packing fraction distribution in the one-third assembly. Thus, ROLLO will vary $a b c d e f$ constants to find an optimal TRISO distribution. The normalization factor normalizes the TRISO distribution based on the defined total packing fraction.

An AHTR one-third assembly with a 0.1 total packing fraction and packing fraction distribution of $PF(x, y) = (0.5 \cdot \sin(1 \cdot x + 1) + 2) \cdot (0.7 \cdot \sin(1.5 \cdot y + 2) + 2) \cdot NF$ results in the packing fraction distribution shown in Figure 5.5a, which corresponds to the one-third assembly with varying TRISO distribution in its fuel cells, shown in Figure 5.5b.



(a) TRISO packing fraction distribution values.

(b) TRISO distribution in one-third assembly model.

Figure 5.5: Advanced High-Temperature Reactor (AHTR) one-third assembly with varying TRISO particle distribution across 10×6 cells based on the sine distributions: $PF(x, y) = (0.5 \cdot \sin(1 \cdot x + 1) + 2) \cdot (0.7 \cdot \sin(1.5 \cdot y + 2) + 2) \cdot NF$. The packing fraction values on the left correspond to the TRISO distribution in the one-third assembly on the right.

Input Parameter Modeling: FLiBe Coolant Channel Shape

For both the AHTR plank and one-third assembly models, I model the variation in coolant channel shape with a sinusoidal-like pattern, using OpenMC's cylinder surfaces functionality. By varying the cylinders' radius, the coolant channel shapes' depth and frequency mimic a sinusoidal pattern. I vary the FLiBe coolant channel shape while holding the total coolant volume constant.

For the AHTR plank, r_{top} and r_{bot} variables control the coolant channel shape on the top and bottom FLiBe channels. Figure 5.6 shows the AHTR plank's coolant channel shape for $r_{top} = 0.2$ and $r_{bot} = 0.3$. Thus, ROLLO will vary r_{top} and r_{bot} to find optimal coolant channel shapes for the AHTR plank model.

For the AHTR one-third assembly, r_1, r_2, r_3, r_4, r_5 variables control the coolant channel shape in the inter-plank FLiBe. Figure 5.7 shows the AHTR one-third assembly's inter-

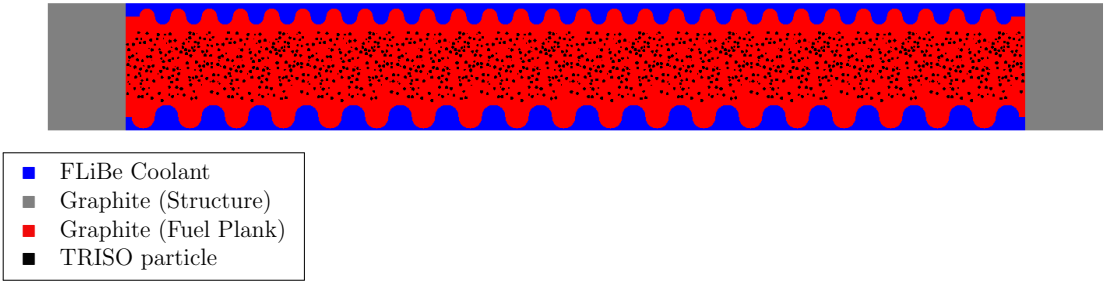


Figure 5.6: Advanced High-Temperature Reactor (AHTR) plank with coolant channel shape variation, $r_{top} = 0.2$ and $r_{bot} = 0.3$.

plank coolant channel shapes for $r_1, r_2, r_3, r_4, r_5 = 0.3, 0.2, 0.1, 0.2, 0.3$. Thus, ROLLO will

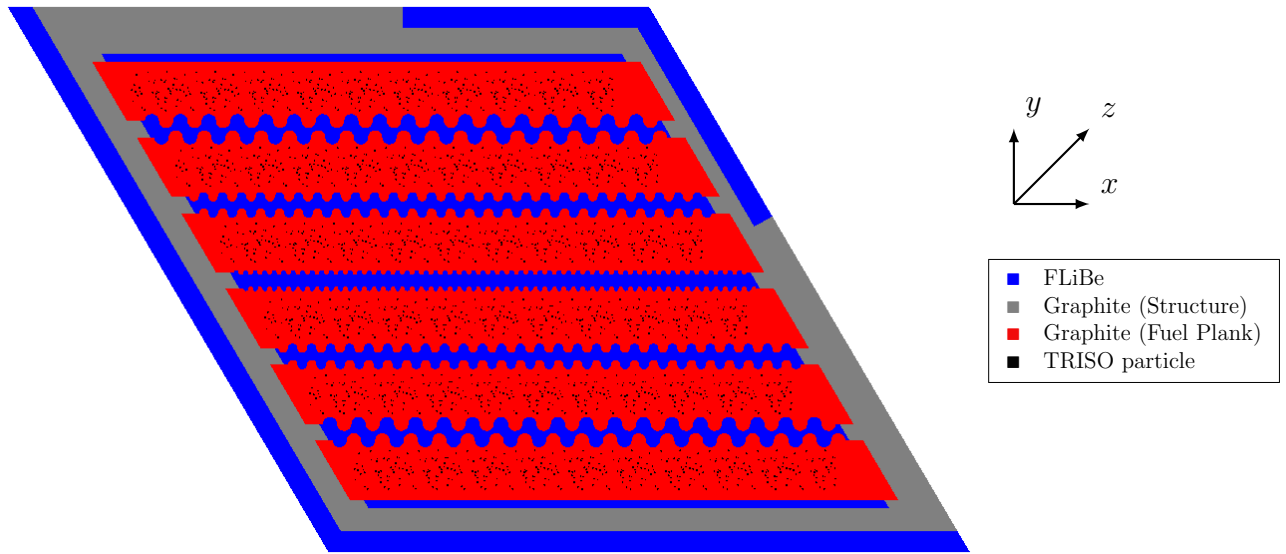


Figure 5.7: Advanced High-Temperature Reactor (AHTR) one-third assembly with coolant channel shape variation, $r_1, r_2, r_3, r_4, r_5 = 0.3, 0.2, 0.1, 0.2, 0.3$.

vary r_1, r_2, r_3, r_4, r_5 to find optimal coolant channel shapes for the AHTR one-third assembly model.

5.3.2 AHTR OpenMC and Moltres Models

The input parameters outlined in the previous section are inputs for the OpenMC neutronics and Moltres temperature models. The Moltres model relies on group constant data produced by the OpenMC model. The OpenMC and Moltres models' workflow:

1. OpenMC neutronics model
2. OpenMC neutronics model produces group constants data for the Moltres model
3. Moltres model mesh generation
4. Moltres temperature model accepts group constants data and mesh

In the subsequent subsections, I describe details and assumptions for each step of the OpenMC and Moltres models' workflow.

AHTR OpenMC Neutronics Model

The OpenMC model template accepts the following input parameters from ROLLO: total packing fraction (PF), TRISO distribution (a, b, c, d, e, f), and FLiBe coolant channel shapes ($r_{top}, r_{bot}, r_1, r_2, r_3, r_4, r_5$). The OpenMC model takes the input parameters and generates an AHTR model with TRISO distribution and FLiBe coolant channel shape variation. A separate OpenMC output file analyzes the OpenMC model's output and calculates the k_{eff} constraint and the objective value: normalized power peaking factor. Section 5.3.3 describes the calculation for each output and constraint value. Figures 5.4, 5.5b, 5.6 are AHTR model snapshots generated by OpenMC.

AHTR Moltres Group Constant Generation

Unlike the OpenMC model, Moltres does not explicitly model each TRISO particle. This is because a TRISO-level fidelity mesh file is impractical and results in extremely long runtimes. Instead, Moltres relies on the OpenMC model to generate group constants data

for the Moltres’ multigroup neutron diffusion calculations. Previously, Moltres could only generate group constant data from Serpent [51] or SCALE [15] output files. I implemented functionality in Moltres for group constant data generation with OpenMC [54].

To enable successful Moltres AHTR temperature model simulations, I established suitable spatial and energy homogenization for group constant generation. These homogenizations preserve accuracy while maintaining an acceptable runtime. For both the AHTR plank and one-third assembly models, I used eight precursor groups and a four-group energy structure derived by Gentry et al. [31] for AHTR geometries. Table 5.3 defines the 4-group energy boundaries.

Table 5.3: 4-group energy structures for Advanced High-Temperature Reactor (AHTR) geometry derived by Gentry et al. [31].

Group Boundaries [MeV]		
Group #	Upper Bound	Lower Bound
1	2.0000×10^1	9.1188×10^{-3}
2	9.1188×10^{-3}	2.9023×10^{-5}
3	2.9023×10^{-5}	1.8554×10^{-6}
4	1.8554×10^{-6}	1.0000×10^{-12}

For spatial homogenization of the straightened AHTR plank and one-third assembly, I used OpenMC’s *cell* domain type to compute multigroup cross sections for different *cells*. For the AHTR plank, I discretized the plank into 13 *cells*: FLiBe, left graphite, right graphite, and ten fuel cells (each cell has a different packing fraction). Figure 5.8 illustrates the AHTR plank’s spatial homogenization for the OpenMC multigroup calculation for group constant generation.

For the AHTR one-third assembly, I discretized the one-third assembly into 70 *cells*: inter-assembly FLiBe, Y-shaped graphite structure, control rod slot FLiBe, inter-plank FLiBe, each graphite plank (6), and ten fuel cells per plank (60). Figure 5.9 illustrates the AHTR one-third assembly’s spatial homogenization for the OpenMC multigroup calculation for group constant generation.

I compared the key neutronics parameters for the continuous OpenMC and multigroup

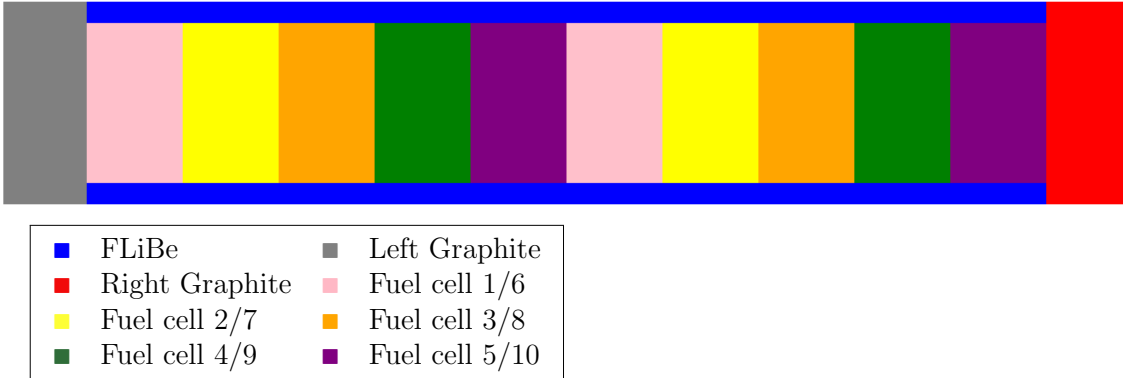


Figure 5.8: Straightened Advanced High-Temperature Reactor (AHTR) fuel plank spatially discretized into 13 *cells* for OpenMC multigroup calculation to produce group constants data for the Moltres model. 13 *cells*: FLiBe, left graphite, right graphite, and ten fuel cells (each cell has a different packing fraction).

Moltres simulations for both the AHTR plank and one-third assembly to ensure that the spatial and energy homogenization preserve accuracy. Section 5.4 reports the verification studies results.

AHTR Moltres Mesh Generation

I wrote Python scripts for the AHTR plank and one-third assembly models that accept the FLiBe coolant channel shape input parameters ($r_{top}, r_{bot}, r_1, r_2, r_3, r_4, r_5$) and generate a geometry script file (.geo) based on the spatial homogenizations outlined in the previous subsection. The AHTR geometry mesh is then generated from the geometry script file using Gmsh [32]. I used Gmsh's *refine by splitting* functionality to refine the mesh. Figures 5.10a and 5.10b show Gmsh rendered geometry file examples generated by the geometry scripts for the AHTR plank and one-third assembly.

AHTR Moltres Temperature Model

The Moltres AHTR Steady-State Temperature Model is a 2D x-y cross-section model of the AHTR plank and one-third assembly. The plank and one-third assembly spatially homogenized geometries are depicted in Figure 5.8 and Figure 5.9. The Moltres temperature

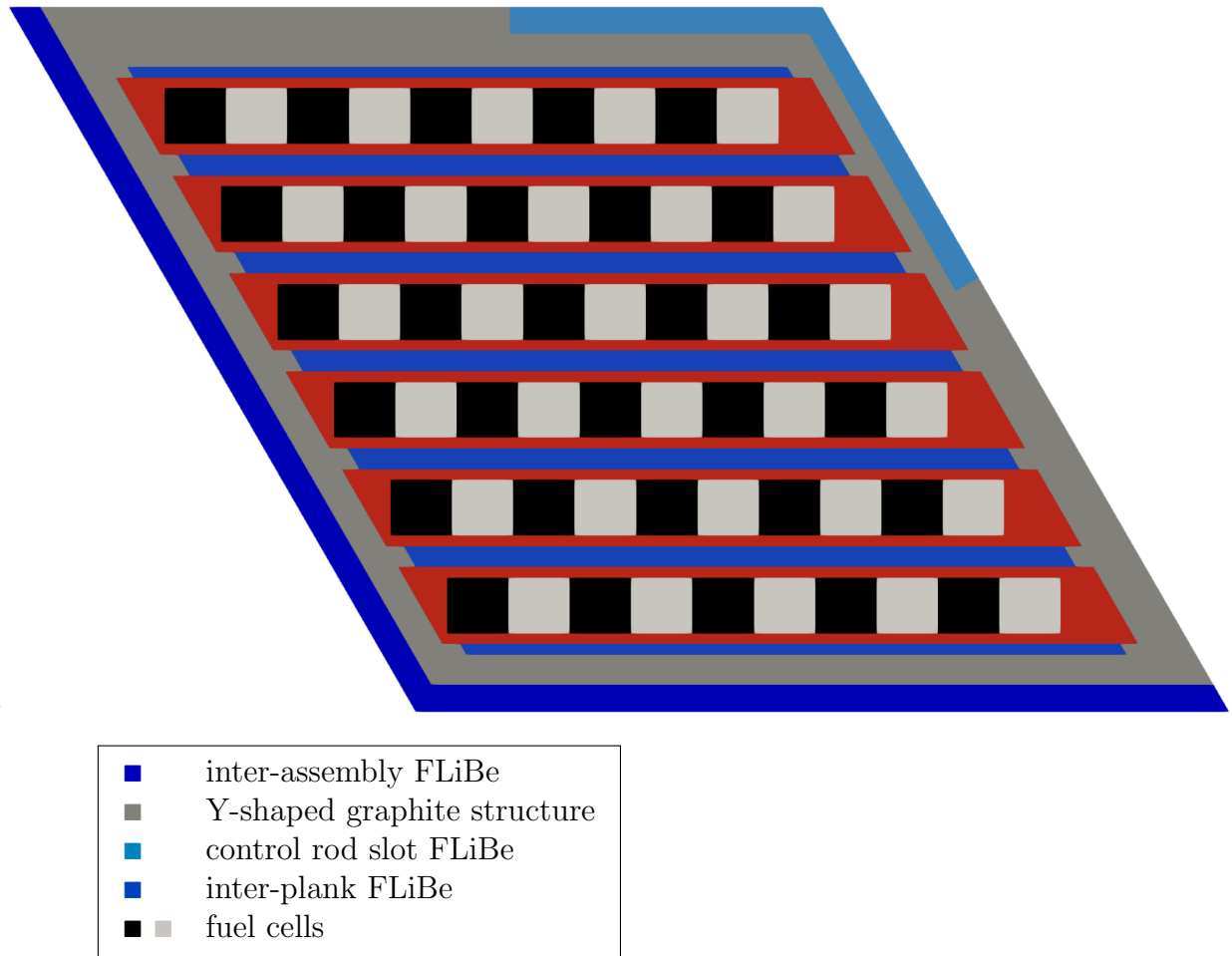
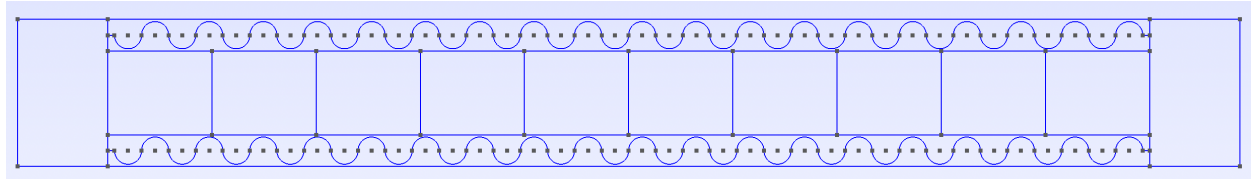
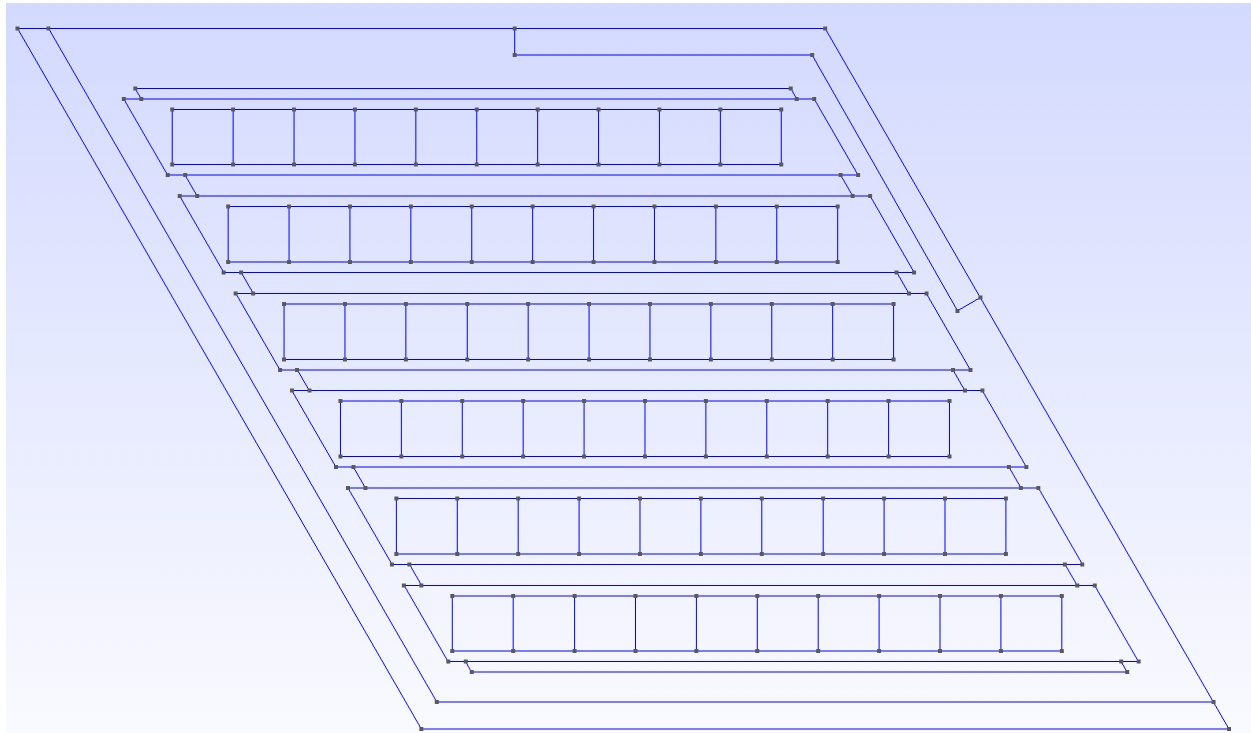


Figure 5.9: Straightened Advanced High-Temperature Reactor (AHTR) one-third assembly spatially discretized into 70 *cells* for OpenMC multigroup calculation to produce group constants data for Moltres model. 70 *cells*: inter-assembly FLiBe, Y-shaped graphite structure, control rod slot FLiBe, inter-plank FLiBe, each graphite plank (6), and ten fuel cells per plank (60).



(a) AHTR plank geometry file



(b) AHTR one-third assembly geometry file

Figure 5.10: Examples of Gmsh rendered geometry files generated by the geometry scripts. These geometry files are meshed using Gmsh, and the mesh files are used in the Moltres temperature models.

model first solves the AHTR neutronics and uses that to solve the AHTR's temperature distribution for a defined power. The temperature model assumes conductive heat transfer throughout the domain and heat removal by uniform salt flow in the coolant region. These assumptions ignore turbulent effects that would most likely be present. However, an in-depth AHTR Moltres model that includes turbulence modeling is out of scope for this dissertation.

Moltres solves the four-group diffusion equations (Equation 2.1) as a steady-state eigenvalue problem to find k_{eff} for the static AHTR models. In the 2D cross-sectional AHTR steady-state temperature model, I ignore the time-dependent and velocity-dependent terms from Moltres' temperature governing equation (Equation 2.2) since it is a steady-state model with no moving fuel, resulting in Equation 5.3:

$$-\nabla \cdot (k_i \nabla T) = Q_i \quad (5.3)$$

where

k_i = thermal conductivity of material i

T = temperature in the model

Q_i = source or sink term in material i

I use insulated temperature boundary conditions. Table 5.4 shows the thermal conductivity values used for each AHTR material.

Table 5.4: Advanced High-Temperature Reactor (AHTR) materials' thermal conductivities used in Moltres temperature models, taken from [71].

Material	Thermal Conductivity [$Wcm^{-1}K^{-1}$]
FLiBe	0.01
Graphite	0.15
Fuel	0.099

Equation 5.4 defines the fuel cells' fission source term (Q_f):

$$Q_f = \sum_{g=1}^G \epsilon_{f,g} \Sigma_{f,g} \phi_g \quad (5.4)$$

where

$$Q_f = \text{source term } \left[\frac{MeV}{cm^3 s} \right]$$

G = number of discrete groups, g [-]

$\epsilon_{f,g}$ = heat produced per fission [MeV]

$\Sigma_{f,g}$ = macroscopic cross section for fission due to neutrons in group g [$\frac{1}{cm}$]

ϕ_g = flux of neutrons in group g [$\frac{n}{cm^2 s}$]

Equation 5.5 defines the heat removal from the AHTR model:

$$Q = h \cdot A \cdot (T(\vec{r}) - T_{ref}) \quad (5.5)$$

where

Q = heat removal rate for 1cm thin slice of the AHTR model [W/cm]

h = heat transfer coefficient [$\frac{W}{cm^3 \cdot K}$]

A = coolant area [cm^2]

$T(\vec{r})$ = temperature at point \vec{r} [K]

T_{ref} = reference temperature [K]

Table 5.5 shows reference temperature and heat transfer coefficient values for the convective heat transfer process.

Table 5.5: AHTR plank and one-third assembly heat transfer constants.

Geometry	Constant	Value	Units	Notes
Plank	h_{plank}	990	$\frac{W}{cm \cdot K}$	Calculated in Eq. 5.6
One-Third Assembly	h_{assem}	611	$\frac{W}{cm \cdot K}$	Calculated in Eq. 5.7
Both	T_{ref}	923	K	AHTR Inlet Temperature [71]

I calculated the heat transfer coefficient (h) for the AHTR plank and one-third assembly using Equation 5.6, 5.7 with the following assumptions:

- AHTR models generate constant amount of power, which is all removed by the coolant
- a linear increase in temperature from inlet to outlet

$$\begin{aligned}
 h_{plank} &= \frac{P_{dz}}{V_{coolant}} \div \Delta T \\
 &= \frac{1456W/cm}{23.1cm \times 0.35cm \times 1cm \times 2} \div 0.0909K/cm \\
 &= 990Wcm^{-3}K^{-1}
 \end{aligned} \tag{5.6}$$

$$\begin{aligned}
 h_{assem} &= \frac{P_{dz}}{V_{coolant}} \div \Delta T \\
 &= \frac{8741W/cm}{157cm^3} \div 0.0909K/cm \\
 &= 611Wcm^{-3}K^{-1}
 \end{aligned} \tag{5.7}$$

and

$$\Delta T = \frac{T_{total}}{H} = \frac{50K}{550cm} = 0.0909K/cm \tag{5.8}$$

where

$$h_{plank} = \text{plank's heat transfer coefficient } [\frac{W}{cm^3 \cdot K}]$$

$$h_{assem} = \text{one-third assembly's heat transfer coefficient } [\frac{W}{cm^3 \cdot K}]$$

P_{dz} = power produced in 1cm AHTR plank/one-third assem Δz slice [W/cm]

$V_{coolant}$ = coolant volume in AHTR plank/one-third assem [cm^3]

ΔT = temperature change across 1cm AHTR Δz slice [K] (5.9)

T_{total} = total temperature change from inlet to outlet [K]

H = AHTR height from inlet to outlet [cm]

The power produced by the AHTR plank and one-third models are calculated based on the FHR benchmark model's specific power of 200 $\frac{W}{gU}$ and the FHR benchmark's TRISO packing fractions in the plank and one-third assembly.

In the ROLLO optimization simulations, I vary the FLiBe coolant channel shape. During the coolant channel shape variation, I hold the coolant volume constant. Since the coolant volume is held constant throughout the coolant channel optimization process, I use the same heat transfer coefficient (h) for all the AHTR Moltres temperature models of varying coolant channel shapes.

5.3.3 Output Parameter Calculation

This section describes how I tallied the AHTR model outputs for the ROLLO optimization problem objectives (described in Table 5.1): total fuel packing fraction, the maximum temperature in the slab, and fuel-normalized power peaking factor.

ROLLO will automatically return the total fuel packing fraction output parameter since it is also an input parameter. In the Moltres AHTR model, I defined a post processor object to return the maximum temperature in the plank. The fuel-normalized power peaking factor output parameter takes into account fuel amount variations across the model. For the AHTR plank and each fuel plank in the AHTR one-third fuel assembly, I discretized the fuel cell area of the plank into 10×5 blocks. I then use OpenMC to tally the fission energy production rate (`fission-q-recoverable` [eV/src]) in each section. I did not normalize

the score to calculate power since the final PPF value is a ratio. Equation 5.10 calculates the fuel-normalized power peaking factor:

$$PPF = \max\left(\frac{fqr_j}{PF_j}\right) \div \text{ave}\left(\frac{fqr_j}{PF_j}\right) \quad (5.10)$$

where

j = discretized fuel area j

PPF = fuel-normalized power peaking factor

fqr_j = fission-q-recoverable at position j

PF_j = fuel packing fraction at position j

5.4 AHTR Moltres Model Verification

In this section, I conduct AHTR Moltres model verification for key neutronics parameters. I set up a criticality eigenvalue problem in Moltres and calculated key neutronics parameters using group constants data from OpenMC. For both the AHTR plank and one-third assembly models, I compare the key neutronics parameters between two simulations:

1. OpenMC simulation with continuous energy and TRISO-level spatial fidelity
2. Moltres simulation with 4-group energy and spatial homogenization

Section 5.3.2 outlined the spatial homogenization used. The OpenMC simulation with TRISO-level fidelity generates the group constants for the energy and spatially homogenized Moltres simulation.

5.4.1 AHTR Plank: Key Neutronics Parameters Verification

This section compares the following key neutronics parameters: effective multiplication factor, reactivity coefficients, flux distribution, and neutron energy spectrum for the AHTR plank model. For this verification study, I used an AHTR plank model with a 0.0979 total packing fraction and packing fraction distribution of $PF(x) = (1.989 \cdot \sin(0.354 \cdot x + 3.143) + 2) \cdot NF$. Figure 5.11 shows the AHTR plank model with TRISO-level fidelity.

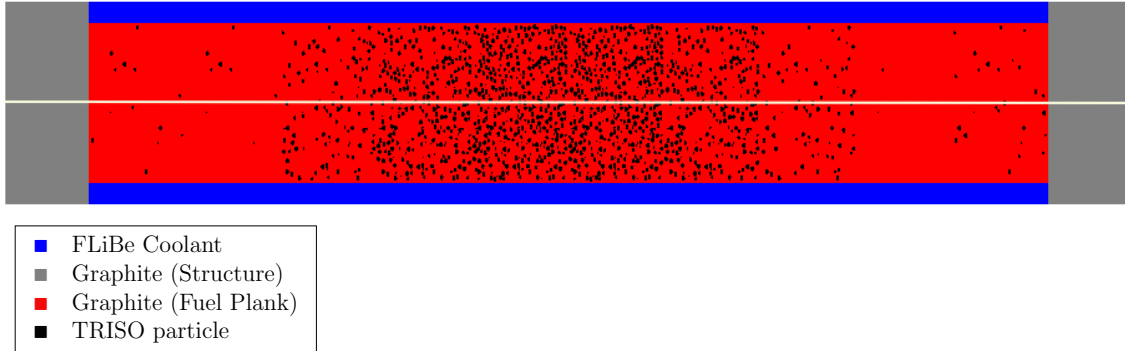


Figure 5.11: Advanced High-Temperature Reactor (AHTR) plank geometry and packing fraction distribution used for AHTR plank's key neutronics parameters verification. The white line corresponds to the centerline where flux distribution is measured.

AHTR Plank: Effective Multiplication Factor

Table 5.6 compares effective multiplication factor for OpenMC simulation with continuous energy and TRISO-level spatial fidelity, OpenMC simulation with 4-group energy and spatial homogenization, and Moltres simulation with 4-group energy and spatial homogenization. I included results from the homogenized OpenMC simulation to distinguish between differences caused by spatial homogenization and energy discretization, or differing OpenMC and Moltres solve methods.

The 50pcm k_{eff} difference between continuous and homogenized OpenMC simulations is within uncertainty, showing that the selected spatial homogenizations and energy discretizations are acceptable. However, there is a 502 pcm difference in the Moltres simulation's

Table 5.6: Advanced High-Temperature Reactor (AHTR) plank's k_{eff} values from the OpenMC simulation with continuous energy and TRISO-level spatial fidelity, OpenMC simulation with 4-group energy and spatial homogenization, and Moltres simulation with 4-group energy and spatial homogenization. All simulations are at 948K. The normalized difference is the pcm difference normalized by OpenMC non-homogenized model's k_{eff} .

Software	Homogenized?	k_{eff}	Difference [pcm]	Normalized Difference [pcm]
OpenMC	No	1.41402 ± 0.00140	-	-
OpenMC	Yes	1.41473 ± 0.00098	+71	+50
Moltres	Yes	1.40696	-706	-502

k_{eff} . A possible reason is that the neutron diffusion method used in Moltres does not approximate this reactor geometry as well. The diffusion coefficients for this reactor type are approximately 1cm. The FLiBe coolant channel has a 0.35cm width which is smaller than the diffusion coefficient, resulting in poor approximations. The k_{eff} values are acceptable since I am not using the Moltres simulation for neutronics modeling but for AHTR plank temperature modeling.

AHTR Plank: Reactivity Coefficients

Moltres' delayed neutron fraction, β_{eff} , is calculated by taking the normalized difference between k_{eff} values with and without delayed neutron precursors (DNPs). Table 5.7 shows that the β_{eff} values from OpenMC and Moltres show excellent agreement with a discrepancy of 0.03pcm. I calculated the temperature reactivity coefficients using Equation 3.1. Temperature reactivity feedback arises mainly from Doppler broadening of resonance absorption peaks and thermal expansion. Table 5.7 also shows that the total temperature coefficients from OpenMC and Moltres have good agreement with a discrepancy of 0.23 pcm/K.

AHTR Plank: Flux Distribution

The $\epsilon_{f,g}$ and $\Sigma_{f,g}$ terms in the Moltres source term (Equation 5.4) are provided to Moltres through the group constants generated by neutronics software, OpenMC. Thus, differences

Table 5.7: AHTR Fuel Plank's β_{eff} values from OpenMC and Moltres simulations at 948K, and total reactivity coefficient values calculated from OpenMC and Moltres at 948K and 1100K. The OpenMC simulation has continuous energy and TRISO-level spatial fidelity and Moltres simulation has 4-group energy and spatial homogenization.

Software	Homogenized?	β_{eff} [pcm]	Diff [pcm]	Total	$\frac{\Delta\rho}{\Delta T}$ [pcm/K]	Diff [pcm/K]
OpenMC	No	654.31	-	-4.26	-	-
Moltres	Yes	654.28	-0.03	-4.49	-0.23	

in the source term between OpenMC and Moltres are dependent on the flux. Comparison of flux distributions produced by Moltres and OpenMC are key to ensuring that Moltres accurately calculates the temperature distribution.

Figure 5.12 shows the 4-group flux distributions for OpenMC and Moltres on the AHTR plank's centerline, along the x-axis at the y-axis' midpoint (white line on Figure 5.11).

The OpenMC simulation shows higher flux in Group 1 and lower flux in Group 2 and 3. There is a good overall agreement for each group's flux.

AHTR Plank: Neutron Energy Spectrum

Figure 5.13 shows the neutron spectrum of the OpenMC simulation for both 252 and 4 groups and the 4-group Moltres simulation. There is good agreement between OpenMC and Moltres models 4-group spectrums.

In summary, Moltres replicated the relevant neutronics parameters with sufficient accuracy using OpenMC's group constant data for the AHTR plank model.

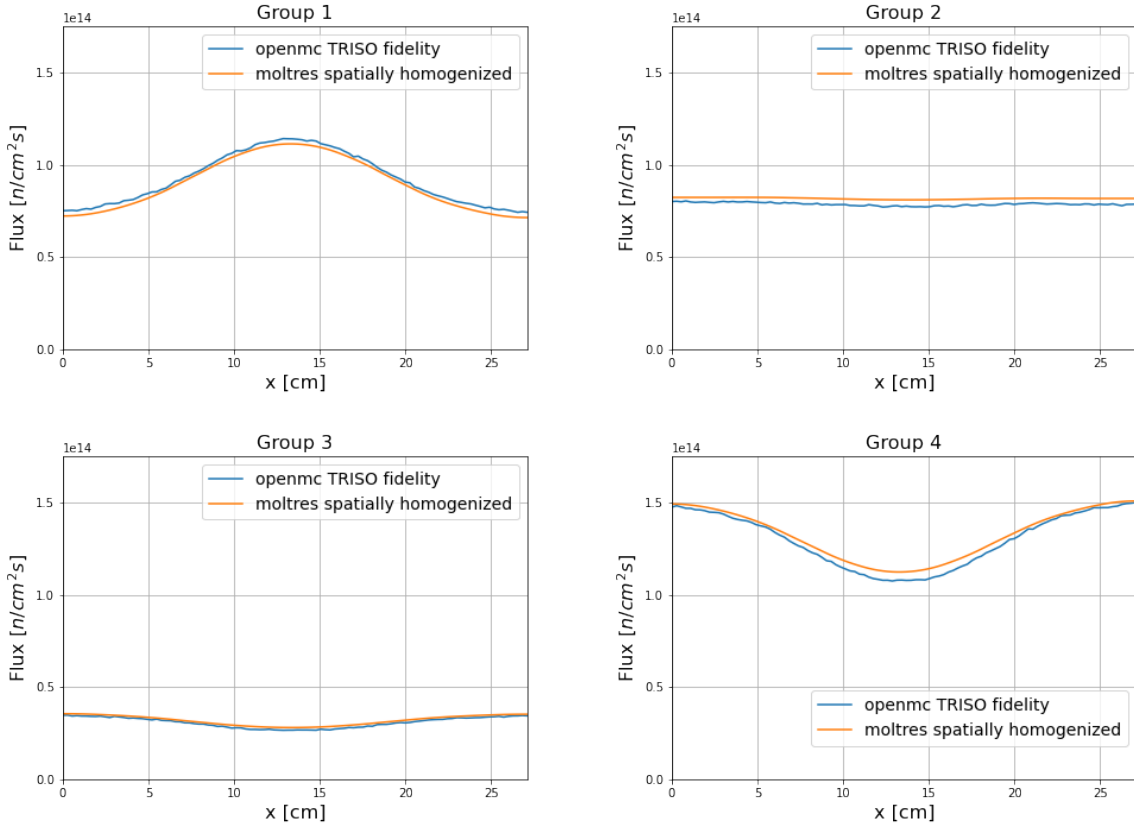


Figure 5.12: Advanced High-Temperature Reactor (AHTR) plank's centerline neutron flux distribution in 4 groups at 948K. Centerline is the white line in Figure 5.11. Comparison is between OpenMC simulation with continuous energy and TRISO-level spatial fidelity and Moltres simulation with 4-group energy and spatial homogenization. Energy Group 1: $E > 9.1188 \times 10^{-3}$ MeV, Energy Group 2: $2.9023 \times 10^{-5} < E < 9.1188 \times 10^{-3}$ MeV, Energy Group 3: $1.8556 \times 10^{-5} < E < 2.9023 \times 10^{-5}$ MeV, Energy Group 4: $1.0 \times 10^{-12} < E < 1.8554 \times 10^{-6}$ MeV.

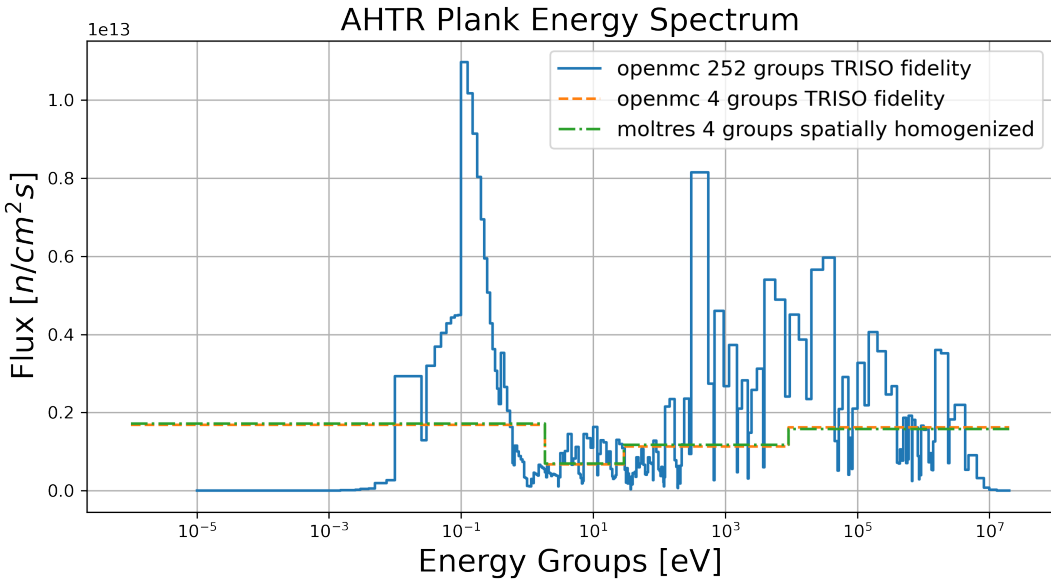


Figure 5.13: Advanced High-Temperature Reactor (AHTR) plank's neutron spectrum. Spectrums include 252 and 4 group spectrums from OpenMC simulation with continuous energy and TRISO-level spatial fidelity and 4 group spectrum from Moltres simulation with 4-group energy and spatial homogenization.

5.4.2 AHTR One-Third Assembly: Key Neutronics Parameters Verification

This section compares the following key neutronics parameters: effective multiplication factor, reactivity coefficients, flux distribution, and neutron energy spectrum for the AHTR one-third assembly model. For this verification study, I used an AHTR one-third assembly model with a constant 0.0979 total packing fraction across all fuel cells. Figure 5.14 shows the AHTR one-third assembly model with TRISO-level fidelity.

AHTR One-Third Assembly: Effective Multiplication Factor

Table 5.8 compares effective multiplication factor for OpenMC simulation with continuous energy and TRISO-level spatial fidelity, OpenMC simulation with 4-group energy and spatial homogenization, and Moltres simulation with 4-group energy and spatial homogenization. I included results from a homogenized OpenMC simulation to distinguish between differ-

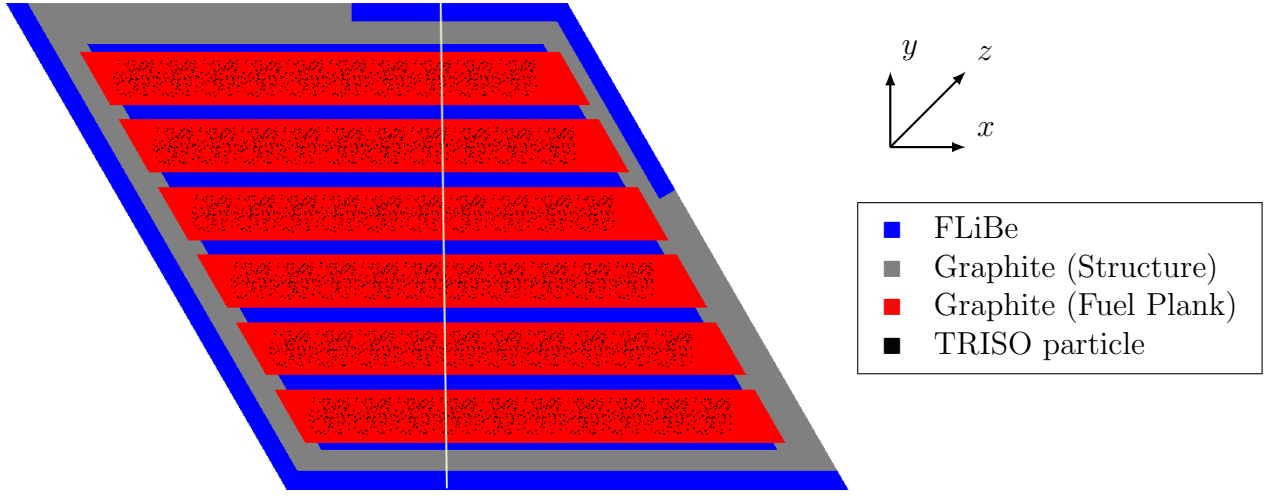


Figure 5.14: AHTR one-third assembly geometry with a constant 0.0979 total packing fraction across all fuel cells used for AHTR one-third assembly's key neutronics parameters verification. The white line corresponds to the centerline where flux distribution is measured.

ences caused by spatial homogenization and energy discretization, or differing OpenMC and Moltres solve methods.

Table 5.8: Advanced High-Temperature Reactor (AHTR) one-third assembly's k_{eff} values from the OpenMC simulation with continuous energy and TRISO-level spatial fidelity, OpenMC simulation with 4-group energy and spatial homogenization, and Moltres simulation with 4-group energy and spatial homogenization. All simulations are at 948K. The normalized difference is the pcm difference normalized by OpenMC non-homogenized model's k_{eff} .

Software	Homogenized?	k_{eff}	Difference [pcm]	Normalized Difference [pcm]
OpenMC	No	1.41657 ± 0.00131	-	-
OpenMC	Yes	1.41670 ± 0.00116	+13	+9
Moltres	Yes	1.40895	-762	-537

The 9pcm k_{eff} difference between continuous and homogenized OpenMC simulations is within uncertainty, showing that the selected spatial homogenizations and energy discretizations are acceptable. However, there is a 537pcm difference in the Moltres simulation's k_{eff} , similar to the AHTR plank model's difference in Section 5.4.1. Again, a possible reason is

that the neutron diffusion method used in Moltres does not approximate this reactor geometry as well. The diffusion coefficients for this reactor type are approximately 1cm. The FLiBe coolant channel has a 0.7cm width which is smaller than the diffusion coefficient, resulting in poor approximations. The k_{eff} values are acceptable since I am not using the Moltres simulation for neutronics modeling but for AHTR one-third assembly temperature modeling.

AHTR One-Third Assembly: Reactivity Coefficients

Moltres' delayed neutron fraction, β_{eff} , is calculated by taking the normalized difference between k_{eff} values with and without DNP. The β_{eff} values from OpenMC and Moltres in Table 5.9 show excellent agreement with a discrepancy of 0.8pcm. I calculated the temperature reactivity coefficients with Equation 3.1. Table 5.9 shows that the total temperature coefficients from OpenMC and Moltres have good agreement with a discrepancy of 0.2 pcm/K.

Table 5.9: AHTR one-third assembly's β_{eff} values from OpenMC and Moltres at 948K, and total reactivity coefficient values calculated from OpenMC and Moltres at 948K and 1100K. The OpenMC simulation has continuous energy and TRISO-level spatial fidelity and Moltres simulation has 4-group energy and spatial homogenization.

Software	Homogenized?	β_{eff} [pcm]	Diff [pcm]	Total	$\frac{\Delta\rho}{\Delta T}$ [pcm/K]	Diff [pcm/K]
OpenMC	No	652.3	-	-3.64	-	
Moltres	Yes	651.5	-0.8	-3.44	+0.2	

AHTR One-Third Assembly: Flux Distribution

The $\epsilon_{f,g}$ and $\Sigma_{f,g}$ terms in the Moltres source term (Equation 5.4) are provided to Moltres through the group constants generated by neutronics software, OpenMC. Thus, differences in the source term between OpenMC and Moltres are dependent on the flux. Comparison of flux distributions produced by Moltres and OpenMC are key to ensuring that temperature distribution is accurately calculated in Moltres.

Figure 5.15 shows the 4-group flux distributions for OpenMC and Moltres on the AHTR one-third assembly's centerline, along the y-axis at the x-axis' midpoint (white line on Figure 5.14).

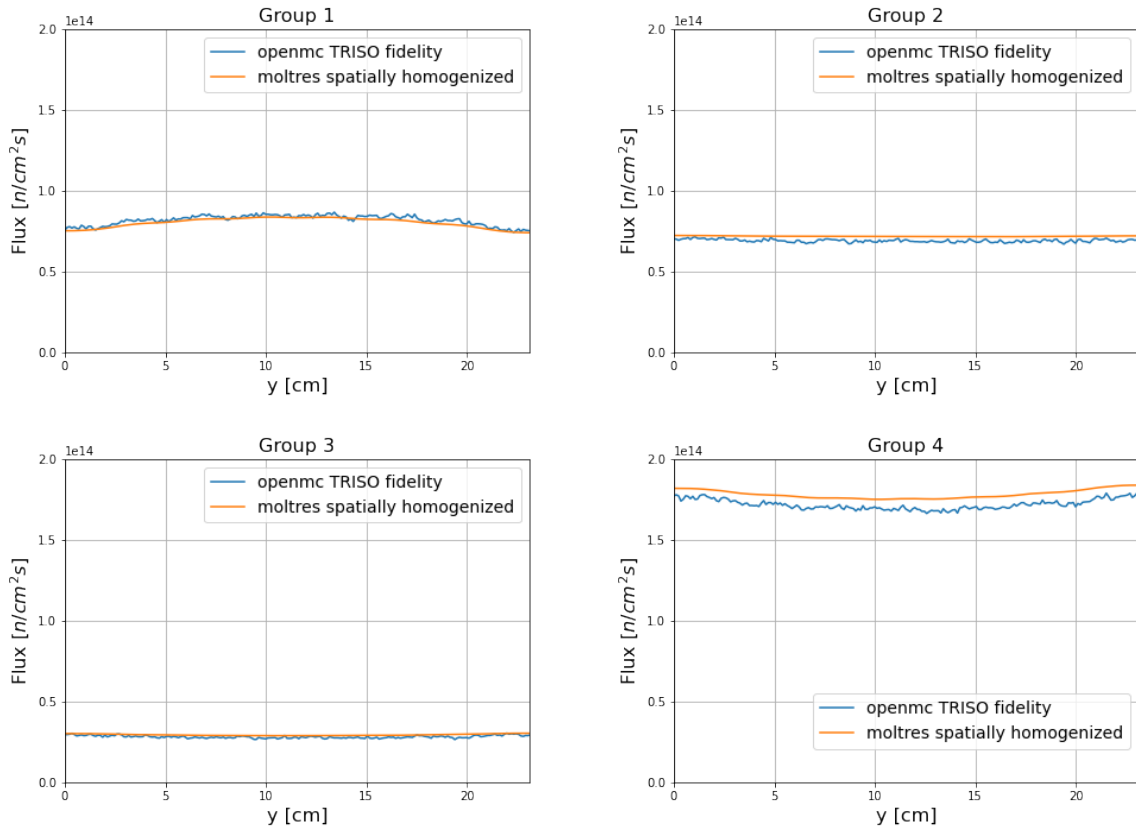


Figure 5.15: Advanced High-Temperature Reactor (AHTR) one-third assembly's centerline neutron flux distribution in 4 groups at 948K. Centerline is the white line in Figure 5.14. Comparison is between OpenMC simulation with continuous energy and TRISO-level spatial fidelity and Moltres simulation with 4-group energy and spatial homogenization. Energy Group 1: $E > 9.1188 \times 10^{-3}$ MeV, Energy Group 2: $2.9023 \times 10^{-5} < E < 9.1188 \times 10^{-3}$ MeV, Energy Group 3: $1.8556 \times 10^{-5} < E < 2.9023 \times 10^{-5}$ MeV, Energy Group 4: $1.0 \times 10^{-12} < E < 1.8554 \times 10^{-6}$ MeV.

The OpenMC simulation shows slightly higher flux in Group 1 and lower flux in Group 2 and 4. There is a good overall agreement for each group's flux.

AHTR One-Third Assembly: Neutron Energy Spectrum

Figure 5.16 shows the one-third assembly's neutron spectrum of the OpenMC simulation for 252 and 4 groups and 4-group Moltres simulation. There is good agreement between

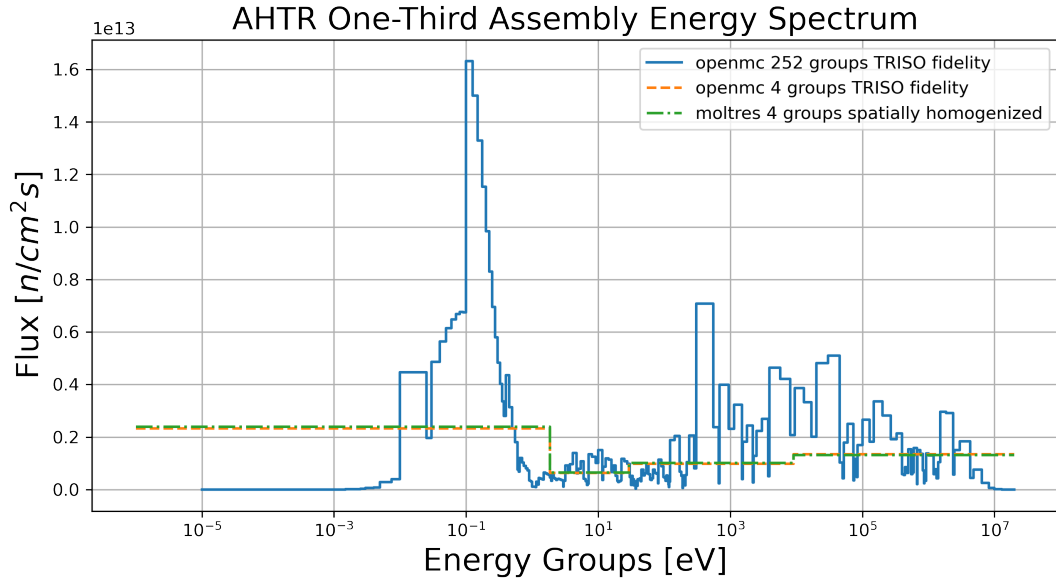


Figure 5.16: Advanced High-Temperature Reactor (AHTR) one-third assembly's neutron spectrum. Spectrums include 252 and 4 group spectrums from OpenMC simulation with continuous energy and TRISO-level spatial fidelity and 4 group spectrum from Moltres simulation with 4-group energy and spatial homogenization.

OpenMC and Moltres models 4-group spectrums.

In summary, Moltres replicated the relevant neutronics parameters with sufficient accuracy using OpenMC's group constant data for the AHTR one-third assembly model.

5.4.3 AHTR Plank and One-Third Assembly: Mesh Refinement

Studies

I performed mesh refinement studies on the AHTR plank and one-third assembly Moltres temperature models to ensure that their geometry mesh inputs are sufficiently converged. Tables 5.10 and 5.11 show the mesh refinement study results for the AHTR plank and one-third assembly. The mesh refinement studies report the average, maximum, and normalized

2-norm temperature difference between refinement steps (Equation 5.11):

$$\|\Delta T_k\|_N = \frac{1}{N} \sqrt{\sum_{i=1}^N (T_{k-1,i} - T_{k,i})^2} \quad (5.11)$$

where

$\|\Delta T_k\|_N$ = normalized 2-norm temperature difference between refinement steps

N = total number of discretized points

k = refinement step

T_{k-1} = temperatures from previous refinement step

T = temperatures from current refinement step

Table 5.10: Advanced High-Temperature Reactor (AHTR) plank's Moltres temperature model's mesh refinement study.

Refinement	Max Plank Temp [K]	Diff [K]	Ave Plank Temp [K]	Diff [K]	$\ \Delta T_k\ _N$
1	1126.219	-	1011.209	-	-
2	1127.711	+1.492	1017.630	+6.421	0.839
3	1128.434	+0.723	1020.021	+2.390	0.313

Table 5.11: Advanced High-Temperature Reactor (AHTR) one-third assembly's Moltres temperature model's mesh refinement study.

Refinement	Max One-Third Assembly Temp [K]	Diff [K]	Ave One-Third Assembly Temp [K]	Diff [K]	$\ \Delta T_k\ _N$
1	1185.436	-	995.963	-	-
2	1186.045	+0.609	1001.751	+5.788	0.703
3	1185.994	-0.051	1003.625	+1.874	0.200
4	1187.658	+1.664	1004.708	+1.083	0.102

Both AHTR plank and one-third assembly show suitable $\|\Delta T_k\|_N$ convergence with more refinement steps. I used x3 mesh refinement for all AHTR plank Moltres temperature models and x4 mesh refinement for all AHTR one-third assembly Moltres temperature

models. Further refinement is unfeasible due to the large mesh size. I am using the Theta supercomputer [3] for the optimization work. Each supercomputer node saves the entire mesh file, further refinement results in mesh sizes that are larger than each Theta node's memory size.

5.4.4 AHTR Plank and One-Third Assembly: Group Constant Temperature Study

During ROLLO optimization, each new reactor model results in the creation of a new Moltres temperature model. Correspondingly, a new set of group constant data needs to be created. Group constant data with multiple temperatures requires running multiple neutronics simulations at the various temperatures, thus, increasing the total compute time required for each new reactor model.

This section explores the effects of using multiple temperature group constant data compared to single temperature group constant data. I set up Moltres AHTR steady-state temperature models for the plank and one-third assembly with group constant data at each and all the of following temperatures: 948, 1024, 1100, and 1200 K. OpenMC AHTR models at the specified temperatures generate the group constant data.

Tables 5.12 and 5.13 show the average and maximum temperature reported by the AHTR plank and one-third assembly Moltres models and their differences compared to the model with group constant data with all four temperatures. Both tables also show the normalized 2-norm of the centerline temperature difference between the AHTR model with all four temperatures and the AHTR models with single temperatures (Equation 5.12):

$$\|\Delta T\|_N = \frac{1}{N} \sqrt{\sum_{i=1}^N (T_{all,i} - T_i)^2} \quad (5.12)$$

where

$\|\Delta T\|_N$ = normalized 2-norm temperature difference

N = total number of discretized points

T_{all} = temperatures from model with group constant data at all four temperatures

T = temperatures from model with group constant data at one temperature

The centerlines for the AHTR plank and one-third models are depicted in Figures 5.11 and 5.14, respectively.

Table 5.12: Advanced High-Temperature Reactor (AHTR) plank's average and maximum temperature and normalized 2-norm of the temperature difference across the plank's centerline for varying group constant temperature data. The difference values are calculated from comparison against the model using group constant data with all four temperatures (All).

Group Constant Data Temps [K]	Ave Plank Temp [K]	Ave Plank Temp Diff [K]	Max Plank Temp [K]	Max Plank Temp Diff [K]	$\ \Delta T\ _N$
All	1019.965	-	1128.306	-	-
948	1019.997	0.032	1128.386	0.080	0.007
1024	1019.989	0.023	1128.640	0.333	0.023
1100	1019.976	0.011	1128.300	-0.006	0.029
1200	1019.943	-0.023	1128.052	-0.255	0.043

The temperature differences between the AHTR plank model with all four temperatures and the AHTR plank models' with each single temperature are not significant. The 948K single temperature group constant data has the lowest 2-norm difference ($\|\Delta T\|_N$). Thus, I use a 948K in the AHTR plank OpenMC neutronics model to generate the group constant data for the Moltres temperature models.

The temperature differences between the AHTR one-third assembly model with all four temperatures and the AHTR plank models' with each single temperature are small ($< 1K$). The 1024K single temperature group constant data has the lowest 2-norm difference ($\|\Delta T\|_N$). Thus, I use 1024K in the AHTR one-third assembly OpenMC neutronics model to generate the group constant data for the Moltres temperature models.

Table 5.13: AHTR one-third assembly's average and maximum temperature and 2-norm of the temperature difference across the slab's centerline for varying group constant temperature data. The difference values are calculated from comparison against the model using group constant data with all four temperatures (All).

Group Constant Data Temps [K]	Ave One-Third Assembly Temp [K]	Diff [K]	Max One-Third Assembly Temp [K]	Diff [K]	$\ \Delta T\ _N$
All	1004.366	-	1186.359	-	-
948	1004.708	+0.341	1187.658	+1.299	0.044
1024	1004.676	+0.310	1187.148	+0.788	0.041
1100	1004.622	+0.256	1186.085	-0.274	0.046
1200	1004.539	+0.172	1185.359	-1.000	0.047

5.5 ROLLO Hyperparameter Tuning

In a ROLLO input file, the user defines hyperparameters for the genetic algorithm. A good hyperparameter set guides the optimization process by balancing exploitation and exploration to find an optimal solution quickly and accurately. Finding a good hyperparameter set requires a trial-and-error process.

The subsequent subsections describe the hyperparameter search I conducted for single-objective and multi-objective optimization.

5.5.1 ROLLO Single-Objective Optimization Hyperparameters

I performed the single-objective hyperparameter search with a coarse-to-fine random sampling scheme, whose advantages I previously discussed in Section 2.4.2. I used an AHTR plank OpenMC model for the hyperparameter search (Figure 5.1). The hyperparameters are population size, number of generations, mutation probability, mating probability, selection operator, selection operator's number of individuals, selection operator's tournament size, mutation operator, and mating operator. I started with 25 coarse experiments and fine-tuned the hyperparameters with 15 more experiments. For each genetic algorithm experiment, OpenMC evaluations remained constant at 600. The number of evaluations correlates with the population size and the number of generations. I randomly sampled population

size and used Equation 5.13 to calculate the number of generations:

$$\text{no. of generations} = \frac{\text{no. of evaluations}}{\text{population size}} \quad (5.13)$$

Table 5.14 shows the lower and upper bounds used for randomly sampling each hyperparameter at each phase of the hyperparameter search.

Table 5.14: Hyperparameter search is conducted in three phases: *Coarse Search*, *Fine Search 1*, *Fine Search 2*. Hyperparameters' lower and upper bounds for each search phase are listed.

Hyperparameter	Type	Coarse Search Bounds	Fine Search 1 Bounds	Fine Search 2 Bounds
Experiments	-	0 to 24	24 to 34	35 to 39
Population size (pop)	Continuous	$10 < x < 100$	$20 < x < 60$	60
Mutation probability	Continuous	$0.1 < x < 0.4$	$0.2 < x < 0.4$	$0.2 < x < 0.3$
Mating probability	Continuous	$0.1 < x < 0.6$	$0.1 < x < 0.3$	$0.45 < x < 0.6$
Selection operator	Discrete	SelTournament, SelBest, SelNSGA2	SelTournament, SelBest, SelNSGA2	SelTournament
Selection individuals	Continuous	$\frac{1}{3}pop < x < \frac{2}{3}pop$	$\frac{1}{3}pop < x < \frac{2}{3}pop$	15
Selection tournament size (only for SelTournament)	Continuous	$2 < x < 8$	$2 < x < 8$	5
Mutation operator	Discrete	mutPolynomialBounded	mutPolynomialBounded	mutPolynomialBounded
Mating operator	Discrete	cxOnePoint, cxUniform, cxBlend	cxOnePoint, cxUniform	cxOnePoint, cxBlend

The initial 25 coarse experiments' sought to narrow down the hyperparameters to find a smaller set of hyperparameter bounds that produce higher k_{eff} values. Figure 5.17 shows the hyperparameters' plot against each other with a third color dimension representing the average k_{eff} value ($\overline{k_{eff}}$) in each experiment's final generation. Lighter scatter points indicate higher final population k_{eff} values, suggesting better hyperparameter sets. I plot the hyperparameters against each other to visualize the interdependence between hyperparameters. From the coarse hyperparameter search (Figure 5.17), I noticed the following trends:

- Mutation probability has a higher $\overline{k_{eff}}$, between 0.2 and 0.4.
- Mating probability has a higher $\overline{k_{eff}}$, between 0.1 and 0.3.

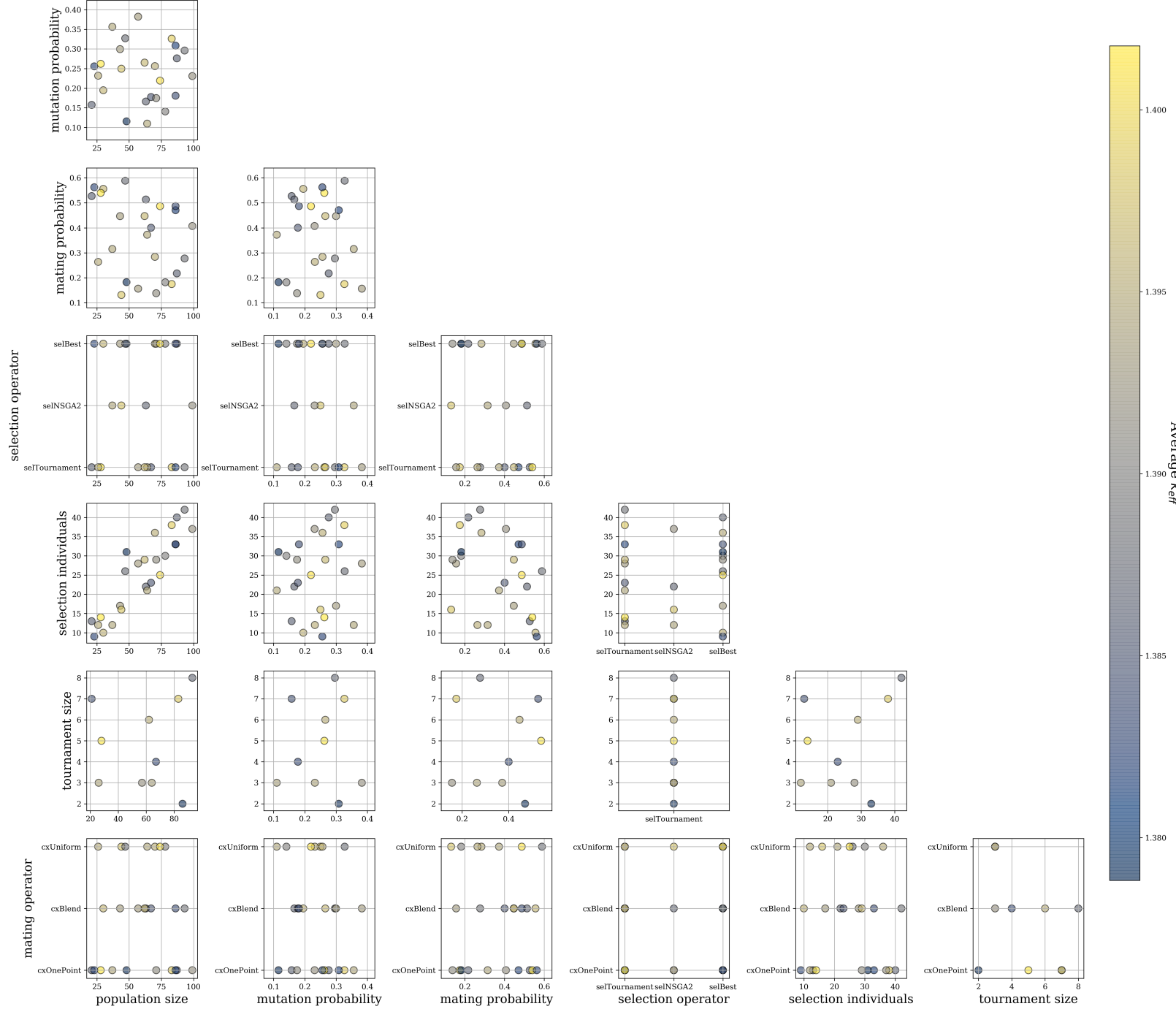


Figure 5.17: Coarse Reactor evOLutionary aLgorithm Optimizer (ROLLO) hyperparameters search's results. Hyperparameter values are plot against each other with a third color dimension representing each experiment's final population's $\overline{k_{eff}}$.

- Population size has a higher \bar{k}_{eff} , between 20 and 60.
- No obvious interdependence between hyperparameters.

Next, I proceeded to the fine searches. From Figure 5.17, I narrowed down population size, mutation probability, and mating probability bounds, as shown in Table 5.14's *Fine Search 1 Bounds* column. I found no significant trends in the other hyperparameters, so I left them as is. I ran ten more experiments (25 to 34), sampling hyperparameters from the *Fine Search 1 Bounds*. From these results, I conducted a second fine search with five experiments (35 to 39) with further tuned hyperparameter bounds, as shown in Table 5.14's *Fine Search 2 Bounds* column. I determined these new hyperparameter bounds based on these reasons:

- Mutation probability has a higher \bar{k}_{eff} , between 0.2 and 0.3.
- I overlooked \bar{k}_{eff} peaking at mating probability between 0.45 and 0.6 in the previous *Fine Search 1*; thus, I shifted the bounds.
- The highest \bar{k}_{eff} occurred for `selTournament`.
- I narrowed down mating operator options to `cxBlend` and `cxOnePoint` since they had higher \bar{k}_{eff} than `cxUniform`.
- I selected arbitrary numbers for population size, selection individuals, and tournament size since they did not correlate with \bar{k}_{eff} values.

Figure 5.18 shows the relationship between hyperparameter values and a , b , c control parameters, final generation k_{effmax} , and final generation \bar{k}_{eff} . The coarse experiments' scatter points are 50% transparent, while the fine experiments' scatter points are opaque. In Figure 5.18, on average, the fine experiments (opaque scatter points) have higher \bar{k}_{eff} , which indicates that the hyperparameter search process met its objective of finding hyperparameter bounds that enable quicker and more accurate optimization.

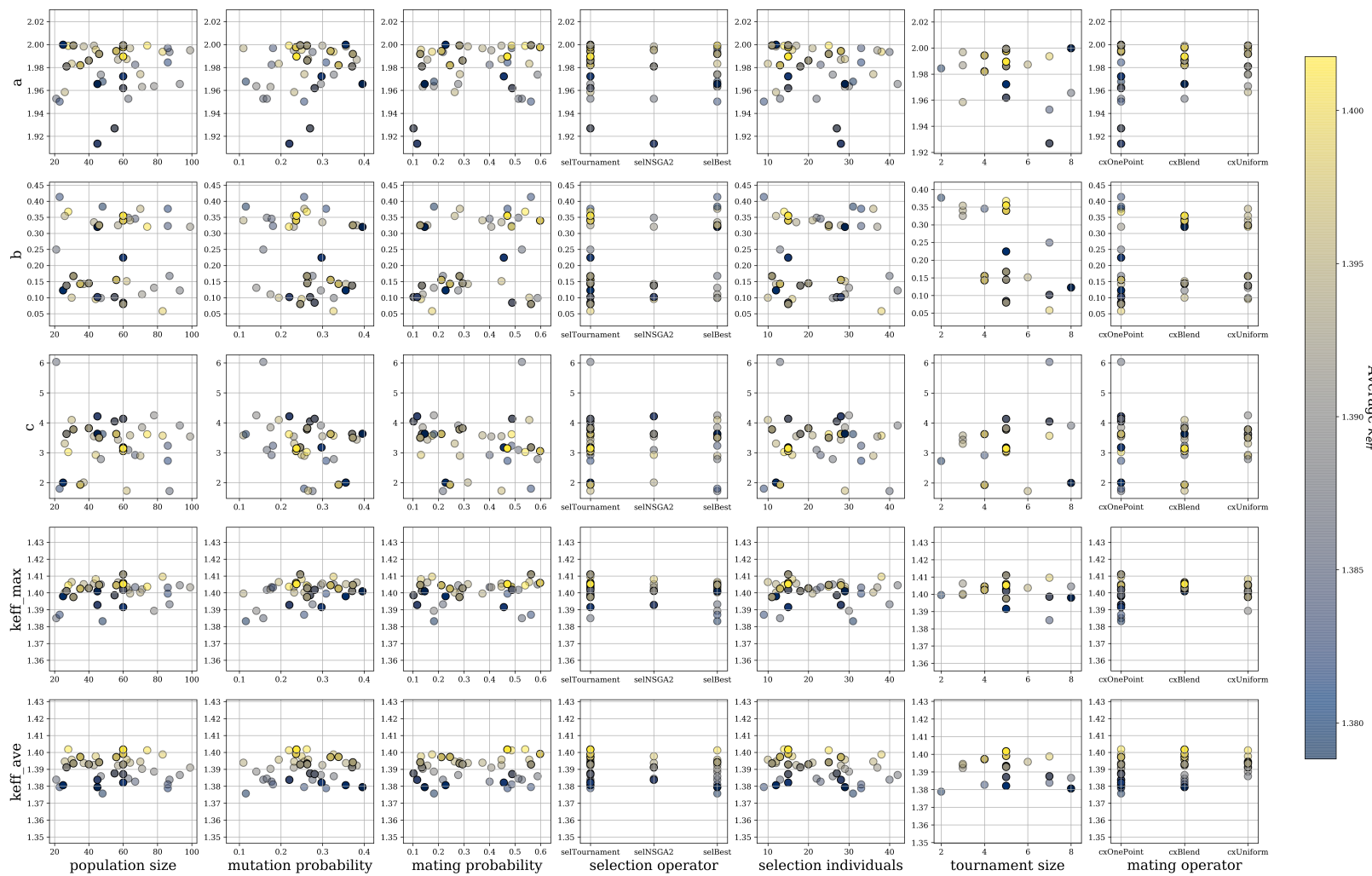


Figure 5.18: Reactor evOLutionary aLgorithm Optimizer (ROLLO) hyperparameters search's results for all 40 experiments (coarse and fine). I plot the hyperparameters against: a,b,c control parameters, each experiment's final generation $k_{eff\ max}$, and final generation \bar{k}_{eff} with a third color dimension representing each experiment's final population's \bar{k}_{eff} (color bar representing the k_{eff} values provided on the right side of the figure). Coarse experiments' (0 to 24) scatter points are 50% transparent, while the fine experiments' (24 to 39) scatter points are opaque.

I ran these hyperparameter search simulations on the BlueWaters supercomputer [59]. In each ROLLO simulation, each generation runs a population size number of individual OpenMC simulations. Each OpenMC simulation takes approximately 13 minutes to run on a single BlueWaters XE node. With approximately 600 OpenMC evaluations per ROLLO simulation, one ROLLO simulation takes about 130 BlueWaters node hours. The hyperparameter search ran 40 ROLLO simulations, thus using approximately 5200 node hours.

Table 5.15 shows the hyperparameters for the five experiments with the highest final generation \bar{k}_{eff} . I define the best-performing hyperparameter set as the experiment that

Table 5.15: Control Parameters, k_{eff} results, and hyperparameter values for the five hyperparameter search experiments with the highest final generation \bar{k}_{eff} .

	Experiment No.				
Control/Output Parameters	6	15	24	36	39
k_{eff} [-]	1.39876	1.40155	1.40118	1.39906	1.40165
k_{effmax} [-]	1.40954	1.40440	1.40365	1.40590	1.40519
a [-]	1.993	1.998	1.999	1.997	1.989
b [$\frac{radians}{cm}$]	0.057	0.367	0.320	0.339	0.354
c [radians]	3.571	3.022	3.615	3.053	3.143
Hyperparameter					
Population size	83	28	74	60	60
Generations	8	22	9	10	10
Mutation probability	0.32	0.26	0.21	0.23	0.23
Mating probability	0.17	0.53	0.48	0.59	0.46
Selection operator	selTournament	selTournament	selBest	selTournament	selTournament
Selection individuals	38	14	25	15	15
Selection tournament size	7	5	-	5	5
Mutation operator	mutPolynomial Bounded	mutPolynomial Bounded	mutPolynomial Bounded	mutPolynomial Bounded	mutPolynomial Bounded
Mating operator	cxOnePoint	cxOnePoint	cxUniform	cxBlend	cxBlend

produces the highest \bar{k}_{eff} in its final generation. *Fine Search 2*'s experiment 39 produces the best performing hyperparameter set, with $\max(k_{eff}) = 1.40519$. Therefore, for single-objective ROLLO optimization simulations in this dissertation, I use the hyperparameter

set from experiment 39.

5.5.2 ROLLO Multi-Objective Optimization Hyperparameters

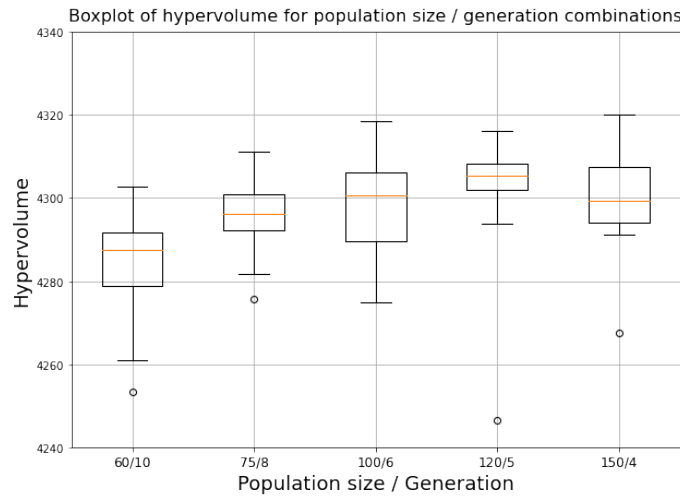
Due to a lack of computational resources, I did not use an OpenMC example problem or a coarse-to-fine random sampling scheme for the multi-objective optimization hyperparameter search. I used the Binh and Korn function described in Section 4.4.2 as an example problem to conduct the hyperparameter search.

I conducted a simpler hyperparameter search for the multi-objective optimization case. I chose to use `SelNSGA2` for the selection operator, since it is an elitist operator that works well for multi-objective optimization. Next, I varied each of the following parameters individually and compared their hypervolume values: population size/generations, mutation probability, and mating probability. Section 4.4.2 describes that the hypervolume indicator quantifies the multi-objective optimization’s Pareto front’s goodness (bigger = better).

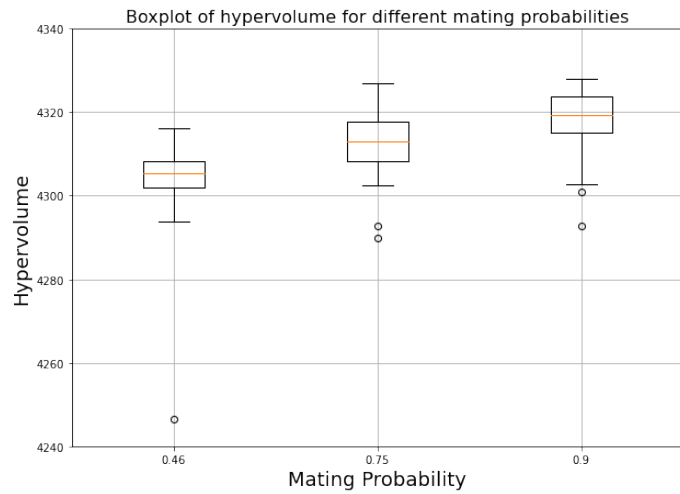
Figure 5.19 shows boxplots comparing hypervolumes for various hyperparameters. I ran each simulation 25 times to produce each box plot. Figure 5.19a shows the boxplot comparing hypervolume for different population size and generation combinations. Similar to Section 5.5.1, I held the total number of OpenMC evaluations constant at 600. Equation 5.13 shows the relationship between population size and generations. The 120-5 population size-generations combination performs the best with the highest hypervolume median (orange line).

Figure 5.19b shows a boxplot comparing hypervolume for different mating probabilities. The 0.9 mutation probability performs the best with the highest hypervolume median (orange line), compared to the 0.46 from the best single-objective hyperparameter set (Section 5.5.1). Figure 5.19c shows a boxplot comparing hypervolume for different mutation probabilities. The 0.23 mating probability from the best single-objective hyperparameter set (Section 5.5.1) performs as well as the 0.1 mating probability.

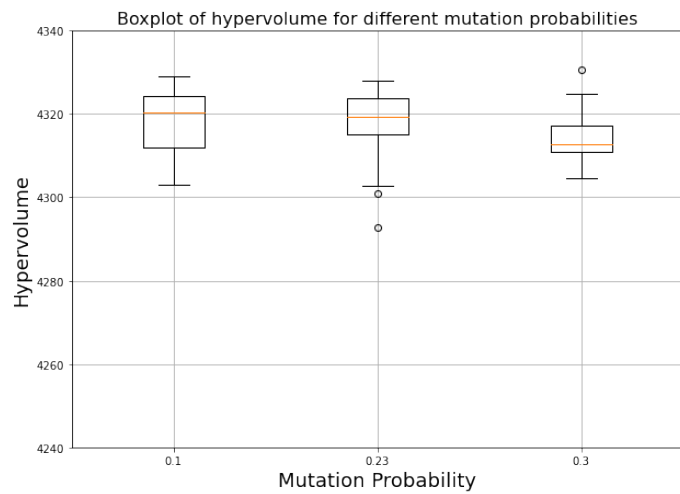
Table 5.16 summarizes the hyperparameters I used for ROLLO multi-objective opti-



(a) Population size / Generation variation.



(b) Mating probability variation



(c) Mutation probability variation

Figure 5.19: Hypervolume comparisons for varying Reactor evOLutionary aLgorithm Optimizer (ROLLO) hyperparameters for the multi-objective optimization hyperparameter search.

mization based on the hyperparameter search.

Table 5.16: Reactor evOLutionary aLgorithm Optimizer (ROLLO) hyperparameters used for multi-objective optimization.

Hyperparameter	Value
Population size	120
Generations	5
Mutation probability	0.9
Mating probability	0.23
Selection operator	<code>SelNSGA2</code>
Mutation operator	<code>mutPolynomial_Bounded</code>
Mating operator	<code>cxBlend</code>

5.6 Summary

This chapter describes the modeling and optimization methodology of the Advanced High-Temperature Reactor (AHTR) plank and one-third assembly optimization for non-conventional geometries and parameters conducted using the Reactor evOLutionary aLgorithm Optimizer (ROLLO) software. I defined and described the AHTR input parameters varied for the optimization problems. The input parameters include Tristructural Isotropic (TRISO) packing distribution, total fuel packing fraction, and coolant channel shape. I defined and motivated the key optimization objectives: minimizing fuel amount, maximizing heat transfer, and minimizing power peaking. I described the AHTR plank and one-third assembly geometries and detailed their modeling workflow: the AHTR input parameter variations, the OpenMC neutronics model, the Moltres temperature model, and the output constraint and objective value calculations. I conducted key neutronics parameter verifications, which confirmed that the spatial and energy homogenizations used for the AHTR plank and one-third assembly Moltres temperature models preserved accuracy. Finally, I described the ROLLO hyperparameter tuning process and reported the hyperparameters used for the single and multi-objective optimization problems.

The following two chapters, the AHTR plank optimization results, and AHTR one-third assembly optimization results, use the described methods.

References

- [1] Fluoride Salt-Cooled High-Temperature Reactor (FHR) Benchmark. URL: https://www.oecd-nea.org/jcms/pl_20249/fluoride-salt-cooled-high-temperature-reactor-fhr-benchmark.
- [2] Roadmap for Regulatory Acceptance of Advanced Manufacturing Methods in the Nuclear Energy Industry. NEI Report, Nuclear Energy Institute. URL: <https://www.nrc.gov/docs/ML1913/ML19134A087.pdf>.
- [3] Theta/ThetaGPU | Argonne Leadership Computing Facility. URL: <https://www.alcf.anl.gov/alcf-resources/theta>.
- [4] Printed titanium parts expected to save millions in Boeing Dreamliner costs. *Reuters*, April 2017. URL: <https://www.reuters.com/article/us-norsk-boeing-idUSKBN17C264>.
- [5] Transformation In 3D: How A Walnut-Sized Part Changed The Way GE Aviation Builds Jet Engines | GE News, 2018. URL: <http://www.ge.com/news/reports/transformation-3d-walnut-sized-part-changed-way-ge-aviation-builds-jet-engines>.
- [6] Argonne Leadership Computing Facility, 2022. URL: <https://www.alcf.anl.gov/>.
- [7] David Ackley. *A connectionist machine for genetic hillclimbing*, volume 28. Springer Science & Business Media, 2012.
- [8] Mohamed Bassi, Eduardo Souza de Cursi, Emmanuel Pagnacco, and Rachid Ellaia. Statistics of the Pareto front in Multi-objective Optimization under Uncertainties. *Latin American Journal of Solids and Structures*, 15, November 2018. Publisher: Associação Brasileira de Ciências Mecânicas. URL: <http://www.scielo.br/j/lajss/a/zF63wFPmYFjmKZ8sWkg6MFy/?format=html&lang=en>, doi:10.1590/1679-78255018.
- [9] C. Behar. Technology roadmap update for generation IV nuclear energy systems. In *OECD Nuclear Energy Agency for the Generation IV International Forum, accessed Jan*, volume 17, pages 2014–03, 2014. Issue: 2018.
- [10] Andrew Bergeron and J. B. Crigger. Early progress on additive manufacturing of nuclear fuel materials. *Journal of Nuclear Materials*, 508:344–347, 2018. ISBN: 0022-3115 Publisher: Elsevier.

- [11] Benjamin R. Betzler, David Chandler, David H. Cook, Eva E. Davidson, and Germina Ilas. Design optimization methods for high-performance research reactor core design. *Nuclear Engineering and Design*, 352:110167, 2019. ISBN: 0029-5493 Publisher: Elsevier.
- [12] B.R. Betzler, B.J. Ade, A.J. Wysocki, P.K. Jain, P.C. Chesser, M.S. Greenwood, and K.A. Terrani. Transformational Challenge Reactor preconceptual core design studies. *Nuclear Engineering and Design*, 367:110781, October 2020. URL: <https://linkinghub.elsevier.com/retrieve/pii/S0029549320302752>, doi:10.1016/j.nucengdes.2020.110781.
- [13] To Thanh Binh and Ulrich Korn. MOBES: A multiobjective evolution strategy for constrained optimization problems. In *The third international conference on genetic algorithms (Mendel 97)*, volume 25, page 27, 1997.
- [14] A. Blanchard, K. R. Yates, J. F. Zino, D. Biswas, S. C. Aiken, D. E. Carlson, H. Hoang, and D. Heemstra. Updated Critical Mass Estimates for Plutonium-238. Technical report, Savannah River Site, 1999.
- [15] J. A. Bucholz. SCALE: A modular code system for performing standardized computer analyses for licensing evaluation. NUREG NUREG/CR-0200-Vol.2-Bk.2; ORNL/NUREG/CSD-2-Vol.2-Bk.2 ON: DE82013370; TRN: 82-013156, Oak Ridge National Lab., TN (USA), 1982. URL: <http://www.osti.gov/scitech/biblio/5360496>.
- [16] Jonathan Byrne, Philip Cardiff, Anthony Brabazon, and Michael O'Neill. Evolving parametric aircraft models for design exploration and optimisation. *Neurocomputing*, 142:39–47, October 2014. URL: <https://linkinghub.elsevier.com/retrieve/pii/S092523121400530X>, doi:10.1016/j.neucom.2014.04.004.
- [17] M. B. Chadwick, M. Herman, P. Obložinský, M. E. Dunn, Y. Danon, A. C. Kahler, D. L. Smith, B. Pritychenko, G. Arbanas, R. Arcilla, R. Brewer, D. A. Brown, R. Capote, A. D. Carlson, Y. S. Cho, H. Derrien, K. Guber, G. M. Hale, S. Hoblit, S. Holloway, T. D. Johnson, T. Kawano, B. C. Kiedrowski, H. Kim, S. Kunieda, N. M. Larson, L. Leal, J. P. Lestone, R. C. Little, E. A. McCutchan, R. E. MacFarlane, M. MacInnes, C. M. Mattoon, R. D. McKnight, S. F. Mughabghab, G. P. A. Nobre, G. Palmiotti, A. Palumbo, M. T. Pigni, V. G. Pronyaev, R. O. Sayer, A. A. Sonzogni, N. C. Summers, P. Talou, I. J. Thompson, A. Trkov, R. L. Vogt, S. C. van der Marck, A. Wallner, M. C. White, D. Wiarda, and P. G. Young. ENDF/B-VII.1 Nuclear Data for Science and Technology: Cross Sections, Covariances, Fission Product Yields and Decay Data. *Nuclear Data Sheets*, 112(12):2887–2996, December 2011. doi:10.1016/j.nds.2011.11.002.
- [18] Gwendolyn Chee. arfc/fhr-benchmark, 2021. URL: <https://github.com/arfc/fhr-benchmark>.

- [19] Gwendolyn J. Y. Chee. Documentation for rollo (Reactor Evolutionary Algorithm Optimizer), 2021. URL: <https://gwenchee.github.io/rollo/>.
- [20] Gwendolyn J. Y. Chee. rollo: Reactor Evolutionary Algorithm Optimizer, May 2021. URL: <https://pypi.org/project/rollo/>.
- [21] Anselmo T. Cisneros and Dan Ilas. Neutronics and Depletion Methods for Parametric Studies of Fluoride Salt Cooled High Temperature Reactors with Slab Fuel Geometry and Multi-Batch Fuel Management Schemes. 2012.
- [22] Kalyanmoy Deb. *Multi-objective optimization using evolutionary algorithms*, volume 16. John Wiley & Sons, 2001.
- [23] Kalyanmoy Deb, Amrit Pratap, Sameer Agarwal, and TAMT Meyarivan. A fast and elitist multiobjective genetic algorithm: NSGA-II. *IEEE transactions on evolutionary computation*, 6(2):182–197, 2002. ISBN: 1089-778X Publisher: IEEE.
- [24] M. I. T. Facilitators, UW Madison Facilitators, and UC Berkeley Facilitators. Fluoride-Salt-Cooled, High-Temperature Reactor (FHR) Development Roadmap and Test Reactor Performance Requirements White Paper. 2013. URL: <http://fhr.nuc.berkeley.edu/wp-content/uploads/2013/08/12-004-FHR-Workshop-4-Report-Final.pdf>.
- [25] C. D. Fletcher and R. R. Schultz. RELAP5/MOD3 code manual. Technical report, Nuclear Regulatory Commission, 1992.
- [26] C. W. Forsberg, K. A. Terrani, L. L. Snead, and Y. Katoh. Fluoride-Salt-Cooled High-Temperature Reactor (FHR) with Silicon-Carbide-Matrix Coated-Particle Fuel. In *Transactions of the American Nuclear Society*, volume 107, page 907, 2012. URL: <http://info.ornl.gov/sites/publications/files/Pub37875.pdf>.
- [27] Charles W. Forsberg, Per F. Peterson, and Paul S. Pickard. Molten-salt-cooled advanced high-temperature reactor for production of hydrogen and electricity. *Nuclear Technology*, 144(3):289–302, 2003. ISBN: 0029-5450 Publisher: Taylor & Francis.
- [28] Félix-Antoine Fortin, François-Michel De Rainville, Marc-André Gardner, Marc Parizeau, and Christian Gagné. DEAP: Evolutionary algorithms made easy. *Journal of Machine Learning Research*, 13(Jul):2171–2175, 2012.
- [29] Christian Gagné and Marc Parizeau. Open BEAGLE: A New Versatile C++ Framework for Evolutionary Computation. In *GECCO Late Breaking Papers*, pages 161–168. Citeseer, 2002.
- [30] Aaron Garrett. inspyred: Bio-inspired Algorithms in Python. URL: <https://pypi.python.org/pypi/inspyred> (visited on 11/28/2016), 2014.
- [31] Cole Andrew Gentry. *Development of a Reactor Physics Analysis Procedure for the Plank-Based and Liquid Salt-Cooled Advanced High Temperature Reactor*. PhD thesis, 2016.

- [32] Christophe Geuzaine and Jean-François Remacle. Gmsh: A 3-D finite element mesh generator with built-in pre- and post-processing facilities. *International Journal for Numerical Methods in Engineering*, 79(11):1309–1331, 2009. eprint: <https://onlinelibrary.wiley.com/doi/pdf/10.1002/nme.2579>. URL: <https://onlinelibrary.wiley.com/doi/abs/10.1002/nme.2579>, doi:10.1002/nme.2579.
- [33] Ian Gibson, David W. Rosen, and Brent Stucker. *Additive manufacturing technologies*, volume 17. Springer, 2014.
- [34] GIF. A Technology Roadmap Updtate for Generation IV Nuclear Energy Systems. Technical Report GIF-002-00, US DOE Nuclear Energy Research Advisory Committee and the Generation IV International Forum, 2002.
- [35] David E. Goldberg. Genetic algorithms in search. *Optimization, and MachineLearning*, 1989. Publisher: Addison Wesley Publishing Co. Inc.
- [36] David E. Goldberg, Kalyanmoy Deb, and Dirk Thierens. Toward a better understanding of mixing in genetic algorithms. *Journal of the Society of Instrument and Control Engineers*, 32(1):10–16, 1993. ISBN: 0453-4662 Publisher: The Society of Instrument and Control Engineers.
- [37] Sherrell R. Greene, Jess C. Gehin, David Eugene Holcomb, Juan J. Carbajo, Dan Ilas, Anselmo T. Cisneros, Venugopal Koikal Varma, William R. Corwin, Dane F. Wilson, and Graydon L. Yoder Jr. Pre-conceptual design of a fluoride-salt-cooled small modular advanced high-temperature reactor (SmAHTR). *Oak Ridge National Laboratory, ORNL/TM-2010/199*, 2010.
- [38] Andreia P. Guerreiro, Carlos M. Fonseca, and Luís Paquete. The Hypervolume Indicator: Problems and Algorithms. *arXiv:2005.00515 [cs]*, May 2020. arXiv: 2005.00515. URL: <http://arxiv.org/abs/2005.00515>.
- [39] M. K. M. Ho, G. H. Yeoh, and G. Braoudakis. Molten salt reactors. In A. Méndez-Vilas, editor, *Materials and processes for energy: communicating current research and technological developments*, number 1 in Energy Book Series, pages 761–768. Formatec Research Center, Badajoz, Spain, 2013 edition, 2013. <http://www.formatec.info/energymaterialsbook/> <http://www.energymaterialsbook.org/chapters.html>.
- [40] David E. Holcomb, George F. Flanagan, Gary T. Mays, W. David Pointer, Kevin R. Robb, and Graydon L. Yoder Jr. Fluoride salt-cooled high-temperature reactor technology development and demonstration roadmap. *ORNL/TM-2013/401, ORNL, Oak Ridge, TN*, 2013.
- [41] David Eugene Holcomb, Dan Ilas, Venugopal Koikal Varma, Anselmo T. Cisneros, Ryan P. Kelly, and Jess C. Gehin. Core and refueling design studies for the advanced high temperature reactor. *ORNL/TM-2011/365, Oak Ridge National Laboratory, Oak Ridge, TN*, 2011.

- [42] Jeremy Jordan. Hyperparameter tuning for machine learning models., November 2017. URL: <https://www.jeremyjordan.me/hyperparameter-tuning/>.
- [43] Sarah Kamalpour and Hossein Khalafi. SMART reactor core design optimization based on FCM fuel. *Nuclear Engineering and Design*, page 110970, 2020. ISBN: 0029-5493 Publisher: Elsevier.
- [44] K. Koebke. A new approach to homogenization and group condensation. Technical report, 1980.
- [45] Takaaki Koyanagi, Kurt Terrani, Shay Harrison, Jian Liu, and Yutai Katoh. Additive manufacturing of silicon carbide for nuclear applications. *Journal of Nuclear Materials*, 543:152577, 2020. ISBN: 0022-3115 Publisher: Elsevier.
- [46] Sivam Krish. A practical generative design method. *Computer-Aided Design*, 43(1):88–100, January 2011. URL: <https://linkinghub.elsevier.com/retrieve/pii/S0010448510001764>, doi:10.1016/j.cad.2010.09.009.
- [47] David J. Kropaczek and Ryan Walden. Constraint annealing method for solution of multiconstrained nuclear fuel cycle optimization problems. *Nuclear Science and Engineering*, 193(5):506–522, 2019. ISBN: 0029-5639 Publisher: Taylor & Francis.
- [48] David J. Kropaczek and Ryan Walden. Large-Scale Application of the Constraint Annealing Method for Pressurized Water Reactor Core Design Optimization. *Nuclear Science and Engineering*, 193(5):523–536, 2019. ISBN: 0029-5639 Publisher: Taylor & Francis.
- [49] David L. Krumwiede, Raluca O. Scarlat, Jae Keun Choi, Tung M. Phan, and Per F. Peterson. Three-dimensional modeling of the pebble-bed fluoride-salt-cooled, high-temperature reactor (PB-FHR) commercial plant design. In *Proceedings of the American Nuclear Society 2013 Winter Meeting*, 2013.
- [50] Akansha Kumar and Pavel V. Tsvetkov. A new approach to nuclear reactor design optimization using genetic algorithms and regression analysis. *Annals of Nuclear Energy*, 85:27–35, November 2015. URL: <https://linkinghub.elsevier.com/retrieve/pii/S0306454915002285>, doi:10.1016/j.anucene.2015.04.028.
- [51] Jaakko Leppanen, Maria Pusa, Tuomas Viitanen, Ville Valtavirta, and Toni Kaltiaisenaho. The Serpent Monte Carlo code: Status, development and applications in 2013. *Annals of Nuclear Energy*, 82:142–150, August 2014. doi:10.1016/j.anucene.2014.08.024.
- [52] Hsun-Chia Lin. *Thermal Hydraulics System-Level Code Validation and Transient Analyses for Fluoride Salt-Cooled High-Temperature Reactors*. PhD thesis, 2020.
- [53] B. A. Lindley, J. G. Hosking, P. J. Smith, D. J. Powney, B. S. Tollit, T. D. Newton, R. Perry, T. C. Ware, and P. N. Smith. Current status of the reactor physics code WIMS and recent developments. *Annals of Nuclear Energy*, 102:148–157, 2017. ISBN: 0306-4549 Publisher: Elsevier.

- [54] Alexander Lindsay. Moltres, software for simulating Molten Salt Reactors, 2017. <https://github.com/arfc/moltres>. URL: <https://github.com/arfc/moltres>.
- [55] Alexander Lindsay, Gavin Ridley, Andrei Rykhlevskii, and Kathryn Huff. Introduction to Moltres: An application for simulation of Molten Salt Reactors. *Annals of Nuclear Energy*, 114:530–540, April 2018. URL: <https://linkinghub.elsevier.com/retrieve/pii/S0306454917304760>, doi:10.1016/j.anucene.2017.12.025.
- [56] Limin Liu, Dalin Zhang, Qing Lu, Kunpeng Wang, and Suizheng Qiu. Preliminary neutronic and thermal-hydraulic analysis of a 2 MW Thorium-based Molten Salt Reactor with Solid Fuel. *Progress in Nuclear Energy*, 86:1–10, January 2016. URL: <https://linkinghub.elsevier.com/retrieve/pii/S0149197015300779>, doi:10.1016/j.pnucene.2015.09.011.
- [57] Robert Macfarlane, Douglas W. Muir, R. M. Boicourt, Albert Comstock Kahler III, and Jeremy Lloyd Conlin. The NJOY nuclear data processing system, version 2016. Technical report, Los Alamos National Lab.(LANL), Los Alamos, NM (United States), 2017.
- [58] Longwei Mei, Xiangzhou Cai, Dazhen Jiang, Jingen Chen, Yuhui Zhu, Yafen Liu, and Xiaohe Wang. The investigation of thermal neutron scattering data for molten salt Flibe. *Journal of Nuclear Science and Technology*, 50(7):682–688, 2013. ISBN: 0022-3131 Publisher: Taylor & Francis.
- [59] NCSA. About Blue Waters: The National Center for Supercomputing Applications at the University of Illinois at Urbana-Champaign, 2017. <http://www.ncsa.illinois.edu/>. URL: <http://www.ncsa.illinois.edu/>.
- [60] Andrew Ng, Kian Katanforoosh, and Younes Bensouda Mourri. Improving Deep Neural Networks: Hyperparameter Tuning, Regularization and Optimization, 2021. URL: <https://www.coursera.org/learn/deep-neural-network>.
- [61] Faisal Y. Odeh and Won Sik Yang. Core design optimization and analysis of the Purdue Novel Modular Reactor (NMR-50). *Annals of Nuclear Energy*, 94:288–299, 2016. ISBN: 0306-4549 Publisher: Elsevier.
- [62] Cláudio MNA Pereira and Celso MF Lapa. Coarse-grained parallel genetic algorithm applied to a nuclear reactor core design optimization problem. *Annals of Nuclear Energy*, 30(5):555–565, 2003. ISBN: 0306-4549 Publisher: Elsevier.
- [63] Cláudio M.N.A. Pereira and Wagner F. Sacco. A parallel genetic algorithm with niching technique applied to a nuclear reactor core design optimization problem. *Progress in Nuclear Energy*, 50(7):740–746, September 2008. URL: <https://linkinghub.elsevier.com/retrieve/pii/S014919700800019X>, doi:10.1016/j.pnucene.2007.12.007.
- [64] Christian S. Perone. Pyevolve: a Python open-source framework for genetic algorithms. *Acm Sigevolution*, 4(1):12–20, 2009.

- [65] B. Petrovic, K. Ramey, I. Hill, E. Losa, M. Elsawi, Z. Wu, C. Lu, J. Gonzales, D. Novog, and G. Chee. Preliminary Results of the NEA FHR Benchmark Phase IA and IB (Fuel Element 2-D Benchmark). In *The International Conference on Mathematics and Computational Methods Applied to Nuclear Science and Engineering, Raleigh, NC*, 2021.
- [66] B Petrovic, K Ramey, and Ian Hill. Benchmark Specifications for the Fluoride-salt High-temperature Reactor (FHR) Reactor Physics Calculations. Technical report, Nuclear Energy Agency, March 2021.
- [67] Bojan Petrovic and Kyle M. Ramey. FHR/AHTR NEA Benchmark, October 2019. URL: http://montecarlo.vtt.fi/mtg/2019_Atlanta/Petrovic1.pdf.
- [68] Farzad Rahnema, David Diamond, Dumitru Serghiuta, and Paul Burke. Phenomena, gaps, and issues for neutronics modeling and simulation of FHRs. *Annals of Nuclear Energy*, 123:172–179, January 2019. URL: <http://www.sciencedirect.com/science/article/pii/S0306454918304572>, doi:10.1016/j.anucene.2018.08.035.
- [69] Farzad Rahnema, Bojan Petrovic, Christopher Edgar, Dingkang Zhang, Pietro Avigni, Michael Huang, and Stefano Terlizzi. The Current Status of the Tools for Modeling and Simulation of Advanced High Temperature Reactor Neutronics Analysis. Technical report, Georgia Institute of Technology, 2015.
- [70] Kyle M. Ramey and Bojan Petrovic. Monte Carlo modeling and simulations of AHTR fuel assembly to support V&V of FHR core physics methods. *Annals of Nuclear Energy*, 118:272–282, August 2018. URL: <https://linkinghub.elsevier.com/retrieve/pii/S0306454918301816>, doi:10.1016/j.anucene.2018.04.003.
- [71] Kyle Michael Ramey. *Methodology for Coupled Reactor Physics, Thermal Hydraulics, and Depletion of a Fluoride Salt-Cooled High-Temperature Reactor (FHR)*. PhD thesis, Georgia Institute of Technology, 2021.
- [72] Gábor Renner and Anikó Ekárt. Genetic algorithms in computer aided design. *Computer-aided design*, 35(8):709–726, 2003.
- [73] Paul K. Romano and Benoit Forget. The OpenMC Monte Carlo particle transport code. *Annals of Nuclear Energy*, 51:274–281, January 2013. URL: <http://www.sciencedirect.com/science/article/pii/S0306454912003283>, doi:10.1016/j.anucene.2012.06.040.
- [74] Paul K. Romano, Nicholas E. Horelik, Bryan R. Herman, Adam G. Nelson, Benoit Forget, and Kord Smith. OpenMC: A state-of-the-art Monte Carlo code for research and development. *Annals of Nuclear Energy*, 82(Supplement C):90–97, August 2015. URL: <http://www.sciencedirect.com/science/article/pii/S030645491400379X>, doi:10.1016/j.anucene.2014.07.048.

- [75] Ronacher. Welcome to Jinja2 - Jinja2 Documentation (2.10), 2018. URL: <http://jinja.pocoo.org/docs/2.10/>.
- [76] Jhonathan Rosales, Isabella J. van Rooyen, and Clemente J. Parga. Characterizing surrogates to develop an additive manufacturing process for U₃Si₂ nuclear fuel. *Journal of Nuclear Materials*, 518:117–128, 2019. ISBN: 0022-3115 Publisher: Elsevier.
- [77] M. W. Rosenthal, P. R. Kasten, and R. B. Briggs. Molten-Salt Reactors - History, Status, and Potential. *Nuclear Applications and Technology*, 8(2):107–117, February 1970. doi:10.13182/NT70-A28619.
- [78] Wagner F. Sacco, Hermes Alves Filho, Nélio Henderson, and Cassiano RE de Oliveira. A Metropolis algorithm combined with Nelder–Mead Simplex applied to nuclear reactor core design. *Annals of Nuclear Energy*, 35(5):861–867, 2008. ISBN: 0306-4549 Publisher: Elsevier.
- [79] Wagner F. Sacco and Cláudio MNA Pereira. Two stochastic optimization algorithms applied to nuclear reactor core design. *Progress in Nuclear Energy*, 48(6):525–539, 2006. ISBN: 0149-1970 Publisher: Elsevier.
- [80] Cédric Sauder. Ceramic matrix composites: nuclear applications. *Ceramic matrix composites: materials, modeling and technology*, pages 609–646, 2014. Publisher: Wiley Online Library.
- [81] Raluca O. Scarlat, Michael R. Laufer, Edward D. Blandford, Nicolas Zweibaum, David L. Krumwiede, Anselmo T. Cisneros, Charalampos Andreades, Charles W. Forsberg, Ehud Greenspan, Lin-Wen Hu, and Per F. Peterson. Design and licensing strategies for the fluoride-salt-cooled, high-temperature reactor (FHR) technology. *Progress in Nuclear Energy*, 77:406–420, November 2014. URL: <http://www.sciencedirect.com/science/article/pii/S0149197014001838>, doi:10.1016/j.pnucene.2014.07.002.
- [82] Raluca O. Scarlat and Per F. Peterson. The current status of fluoride salt cooled high temperature reactor (FHR) technology and its overlap with HIF target chamber concepts. *Nuclear Instruments and Methods in Physics Research Section A: Accelerators, Spectrometers, Detectors and Associated Equipment*, 733:57–64, 2014. ISBN: 0168-9002 Publisher: Elsevier. URL: <http://www.sciencedirect.com/science/article/pii/S0168900213007055>, doi:10.1016/j.nima.2013.05.094.
- [83] N. D. See, S. Cetiner, and B. R. Betzler. Design Optimization of the Transformational Challenge Reactor Outlet Plenum. *Nuclear Science and Engineering*, pages 1–20, January 2022. URL: <https://www.tandfonline.com/doi/full/10.1080/00295639.2021.2011571>, doi:10.1080/00295639.2021.2011571.
- [84] SFU. Ackley Function. URL: <https://www.sfu.ca/~ssurjano/ackley.html>.
- [85] Herbert A. Simon. *The sciences of the artificial*. MIT press, 2019.

- [86] Joseph Simpson, James Haley, Corson Cramer, Olivia Shafer, Amy Elliott, Bill Peter, Lonnie Love, and Ryan Dehoff. CONSIDERATIONS FOR APPLICATION OF ADDITIVE MANUFACTURING TO NUCLEAR REACTOR CORE COMPONENTS. page 43, May 2019.
- [87] Robert Smallshire. multiprocessing_on_dill 3.5.0a4 : A friendly fork of multiprocessing which uses dill instead of pickle. URL: https://github.com/sixty-north/multiprocessing_on_dill.
- [88] Lance L. Snead, Takashi Nozawa, Yutai Katoh, Thak-Sang Byun, Sosuke Kondo, and David A. Petti. Handbook of SiC properties for fuel performance modeling. *Journal of nuclear materials*, 371(1-3):329–377, 2007. ISBN: 0022-3115 Publisher: Elsevier.
- [89] Vladimir Sobes, Briana Hiscox, Emilian Popov, Marco Delchini, Richard Archibald, Paul Laiu, Ben Betzler, and Kurt Terrani. ARTIFICIAL INTELLIGENCE DESIGN OF NUCLEAR SYSTEMS EMPOWERED BY ADVANCED MANUFACTURING. page 8, 2020.
- [90] Niyanth Sridharan, Maxim N. Gussev, and Kevin G. Field. Performance of a ferritic/martensitic steel for nuclear reactor applications fabricated using additive manufacturing. *Journal of Nuclear Materials*, 521:45–55, 2019. ISBN: 0022-3115 Publisher: Elsevier.
- [91] ASTM Standard. Standard terminology for additive manufacturing technologies. *ASTM International F2792-12a*, 2012.
- [92] X-5 Monte Carlo Team. MCNP — A General Monte Carlo N-Particle Transport Code, Version 5. Technical Report LA-UR-03-1987, LANL, Los Alamos, NM, April 2003.
- [93] K. A. Terrani. Transformational Challenge Reactor demonstration program. Technical report, 2019. URL: Retrieved from <http://tcr.ornl.gov>.
- [94] Kurt A. Terrani, J. O. Kiggans, Chinthaka M. Silva, C. Shih, Yutai Katoh, and Lance Lewis Snead. Progress on matrix SiC processing and properties for fully ceramic microencapsulated fuel form. *Journal of Nuclear Materials*, 457:9–17, 2015. ISBN: 0022-3115 Publisher: Elsevier.
- [95] Mina Torabi, A. Lashkari, Seyed Farhad Masoudi, and Somayeh Bagheri. Neutronic analysis of control rod effect on safety parameters in Tehran Research Reactor. *Nuclear Engineering and Technology*, 50(7):1017–1023, 2018. ISBN: 1738-5733 Publisher: Elsevier.
- [96] Michael P. Trammell, Brian C. Jolly, M. Dylan Richardson, Austin T. Schumacher, and Kurt A. Terrani. Advanced Nuclear Fuel Fabrication: Particle Fuel Concept for TCR. Technical report, 2019.

- [97] P.J. Turinsky, R.M.K. Al-Chalabi, P. Engrand, H.N. Sarsour, F.X. Faure, and W. Guo. NESTLE: Few-group neutron diffusion equation solver utilizing the nodal expansion method for eigenvalue, adjoint, fixed-source steady-state and transient problems. Technical Report EGG-NRE-11406, 10191160, June 1994. URL: <http://www.osti.gov/servlets/purl/10191160-pnc6Jn/webviewable/>, doi:10.2172/10191160.
- [98] Adrián Uriondo, Manuel Esperon-Miguez, and Suresh Perinpanayagam. The present and future of additive manufacturing in the aerospace sector: A review of important aspects. *Proceedings of the Institution of Mechanical Engineers, Part G: Journal of Aerospace Engineering*, 229(11):2132–2147, 2015. ISBN: 0954-4100 Publisher: SAGE Publications Sage UK: London, England.
- [99] Venugopal Koikal Varma, David Eugene Holcomb, Fred J. Peretz, Eric Craig Bradley, Dan Ilas, A. L. Qualls, and Nathaniel M. Zaharia. AHTR mechanical, structural, and neutronic preconceptual design. Technical report, Oak Ridge National Lab.(ORNL), Oak Ridge, TN (United States), 2012.
- [100] Dingkang Zhang and Farzad Rahnema. Integrated Approach to Fluoride High Temperature Reactor Technology and Licensing Challenges (FHR-IRP). Technical report, Georgia Inst. of Technology, Atlanta, GA (United States), 2019.
- [101] Y. Zhu and A. I. Hawari. Thermal neutron scattering cross section of liquid FLiBe. *Progress in Nuclear Energy*, 101:468–475, 2017. ISBN: 0149-1970 Publisher: Elsevier.